ACCSCIENCE PUBLISHING

International Journal of Bioprinting

RESEARCH ARTICLE

PLA-based bone tissue engineering scaffolds incorporating hydroxyapatite and bioactive glass using digital light processing

Engin Gepek[1,2,3], Fateme Fayyazbakhsh[2,4,5]*, Lev Suliandziga[2], Vadym N. Mochalin[6,7], Osman Iyibilgin[8,9], Yue-Wern Huang[5,10], and Ming C. Leu[2,4,5]

[1]Institute of Natural Sciences, Sakarya University, Sakarya, Turkey

[2]Department of Mechanical and Aerospace Engineering, Missouri University of Science and Technology, Rolla, Missouri, USA

[3]Mechanical Engineering Department, Turkish-German University, Istanbul, Turkey

[4]Intelligence System Center, Missouri University of Science and Technology, Rolla, Missouri, USA

[5]Center for Biomedical Research, Missouri University of Science and Technology, Rolla, Missouri, USA

[6]Department of Chemistry, Missouri University of Science and Technology, Rolla, Missouri, USA

[7]Department of Materials Science and Engineering, Missouri University of Science and Technology, Rolla, Missouri, USA

[8]Biomaterials, Energy, Photocatalysis, Enzyme Technology, Nano & Advanced Materials, Additive Manufacturing, Environmental Applications and Sustainability Research & Development Group (BIOEAMS R&D Group), Sakarya University, Sakarya, Turkey

[9]Mechanical Engineering Department, School/Faculty, Sakarya University, Sakarya, Turkey

[10]Department of Biological Sciences, Missouri University of Science and Technology, Rolla, Missouri, USA

***Corresponding author:**
Fateme Fayyazbakhsh
(f.fba@mst.edu)

Citation: Gepek E, Fayyazbakhsh F, Suliandziga L, et al. PLA-based bone tissue engineering scaffolds incorporating hydroxyapatite and bioactive glass using digital light processing. *Int J Bioprint*. 2025;11(2):573-598. doi: 10.36922/IJB025040029

Received: January 21, 2025
Revised: February 25, 2025
Accepted: February 26, 2025
Published Online: February 26, 2025

Abstract

Bone tissue engineering (BTE) aims to repair bone defects using biocompatible materials with tailored geometries and pore structures, providing appropriate mechanical support and control over biodegradation kinetics to promote bone growth. In this study, we utilized digital light processing (DLP) 3D printing to fabricate scaffolds with varying pore sizes using polymer–ceramic slurries composed of polylactic acid (PLA) as the main polymer matrix, incorporated with hydroxyapatite (HA) and bioactive borate glass (BBG) at various ratios. We studied the effect of composition on rheological behavior, printability, mechanical properties, bioactivity, degradation rate, and biocompatibility. While HA increased viscosity and reduced printing accuracy, it also improved mechanical properties and bioactivity. BBG increased the hydrophilicity and shape fidelity of the scaffold. Both HA and BBG enhanced the compressive mechanical properties by reinforcing the polymer matrix with ceramic particles. To study the scaffold's bioactivity, samples were immersed in simulated body fluid for 4 weeks. Both ceramic additives enhanced the bioactivity of PLA scaffolds, evidenced by the formation of a secondary HA layer on the scaffold surface. Among the scaffolds studied, PLA-BBG exhibited the highest osteocyte viability, followed by PLA-HA and then plain PLA samples. Our findings highlight the potential of DLP 3D printing for the fabrication of tailored polymer–ceramic scaffolds for BTE and other biomedical applications.

Keywords: Bioactivity; Bioactive borate glass; Biodegradation; Bone tissue engineering; Digital light processing; Hydrophilicity; Hydroxyapatite; Polylactic acid

1. Introduction

Bone is the primary component of the mammalian skeletal system, serving key roles in motor function and the protection of internal organs.[1,2] Bone defects are caused by trauma, inflammatory and infectious diseases, congenital malformations, tumor resection, osteoporosis, and bone loss associated with tooth extraction or periodontal disease.[3] Critical bone defects surpass the body's natural healing capabilities and require medical intervention for regeneration. Despite advances in treatment outcomes, managing critical bone defects remains a significant challenge in clinical practice. Globally, over 2 million bone grafts take place each year (with approximately 500,000 in the United States), making bone the second most common transplant tissue after blood.[4,5] Autografts, the gold standard for treating critical bone defects, are limited by donor site morbidity, low availability, and prolonged recovery times. Allografts, while readily available, carry risks of immune rejection, infection, and poor integration. Synthetic grafts and bone cement often lack the bioactivity and mechanical robustness for effective bone regeneration, particularly in load-bearing bones.[6–9] Bone tissue engineering (BTE) has emerged as a promising approach to address critical bone defects by developing scaffolds that mimic bone's extracellular matrix, providing structural support, guiding cell attachment and proliferation, and delivering biochemical cues to enhance osteogenesis.

Besides biocompatibility and bioactivity, BTE scaffolds should be adequately porous to provide vascularization, mechanical strength in the range of surrounding bone, and degradation kinetics aligned with bone regeneration, supporting the fragile healing tissue.[10–12] Traditional methods such as solvent casting, particulate leaching, freeze-drying, gas foaming, and electrospinning have been extensively employed in BTE scaffold fabrication due to their simplicity and scalability.[13,14] However, these techniques face significant limitations, such as material constraints, restricted customization, limited precision in controlling geometry and porosity, and poor reproducibility.[12,15–17] Additionally, traditional fabrication methods often fall short in replicating the intricate 3D architecture of vascularized bone and the spatial distribution of osteogenic cues essential for successful tissue regeneration.[6–9,18,19]

Advancements in 3D printing (additive manufacturing) over the past two decades have significantly enhanced scaffold fabrication by enabling precise control over geometry, pore architecture, and material composition. Continuous improvements in printing resolution, material versatility, and process optimization now allow for the fabrication of highly customized, patient-specific bone scaffolds with tailored mechanical and biological properties.[20–25] Various advanced manufacturing methods like vat photopolymerization, powder bed fusion, binder jetting, material extrusion, and directed energy deposition have been employed to fabricate porous scaffolds for BTE.[21,26–29] Among these, vat photopolymerization methods, including stereolithography (SLA) and digital light processing (DLP), stand out for their ability to create intricate geometries with high precision and resolution. DLP, in particular, can selectively cure an entire resin layer simultaneously, enabling fast processing, while maintaining excellent surface finish and shape fidelity with micron-level precision. Its compatibility with a broad range of biocompatible materials, including polymers and ceramic composites, establishes DLP as a versatile platform for functional scaffold development.[30,31] While both fused filament fabrication (FFF) and DLP can be utilized for scaffold fabrication, DLP offers distinct advantages in terms of resolution, geometric precision, and surface finish. The photopolymerization process in DLP enables the creation of complex, highly interconnected pore architectures with minimal geometric distortion, whereas FFF is limited by filament extrusion constraints, which can result in inconsistent pore sizes, surface roughness, and reduced shape fidelity.[32] Additionally, DLP provides greater control over mechanical properties through modulation of crosslinking density and photopolymerization parameters, an aspect not achievable in FFF due to its reliance on layer adhesion and extrusion settings.

Biomimetic polymer–ceramic scaffolds combine the polymer's flexibility and biodegradability with the ceramic's bioactivity and mechanical strength, mimicking the structure and properties of natural bone.[15] The polymer matrix provides a supportive framework, facilitating cell attachment and proliferation, while the ceramic phase, such as hydroxyapatite (HA), bioactive borate glass (BBG), nanodiamond, clays, etc., enhances osteoinductive and osteoconductive properties, promoting bone mineralization and regeneration.[33–40] Integrating bioactive ceramics such as HA and BBG into photopolymerizable resins enables DLP fabrication of scaffolds with precisely tailored structural and functional properties. This approach, however,

requires slurry to exhibit optimal rheological behavior and curing characteristics for uniform ceramic dispersion, consistent layer curing, and accurate scaffold geometry.[41] Excessive ceramic content can increase viscosity, impeding self-leveling, and potentially causing printing failures. Zhang et al.[42] obtained well-controlled multi-level porous scaffolds by blending calcium phosphate bioceramics with a photosensitive resin composed of polyethylene glycol diacrylate and urethane acrylate. The sintered scaffolds enhanced bone regeneration and osteoinduction in an ectopic preclinical model. In another study, Wang et al.[43] used DLP to fabricate porous biphasic calcium phosphate (BCP) bioceramic scaffolds with ~56.3 vol% porosity and a compressive strength of ~20.07 ± 2.09 MPa.

Polylactic acid (PLA) is an FDA-approved[44] biopolymer. It has been widely used in BTE due to its biocompatibility, tunable biodegradability, and favorable mechanical properties.[5,45,46] An effective approach to overcome PLA's hydrophobicity and limited reactivity, which restricts cell adhesion and scaffold integration with surrounding tissues,[18,47,48] is to combine PLA with bioactive materials that can enhance its surface properties, bioactivity, and cellular interactions.[49] HA, the mineral content of natural bone, is a calcium phosphate-based material with exceptional biocompatibility, bioactivity, and osteoconductive properties, which supports bone ingrowth by forming direct chemical bonds with living tissues.[50] HA contributes to scaffold stiffness and promotes osteointegration. However, low solubility and brittleness limit its standalone use in load-bearing applications.[51] In contrast, BBG is a highly reactive glass that releases various therapeutic ions, including calcium, sodium, magnesium, copper, and zinc, which are essential for promoting bone growth and angiogenesis.[51,52] Ions released from BBG interact with surrounding tissues and biological fluids to form a biologically active calcium phosphate layer on the scaffold surface, promoting strong bonding with the surrounding bone tissue and osteointegration.[53,54] While BBG exhibits excellent bioactivity and biodegradability, its rapid degradation can lead to mechanical instability, resulting in suboptimal bone regeneration.[55–58]

Most research on DLP-printed BTE scaffolds has focused on bioceramics, with few studies exploring the fabrication of polymer–ceramic composite scaffolds.[59,60] The present paper integrates PLA, HA, and BBG for DLP 3D printing, allowing for control over scaffold geometry, pore architecture, and material distribution and leveraging the osteoconductive properties of HA, the bioactivity and angiogenic potential of BBG, and the structural versatility of PLA.

In this study, PLA-based scaffolds for bone regeneration, incorporating HA and BBG, were fabricated using DLP 3D printing. We studied the effects of formulation and design on the physical properties of DLP-printed polymer–ceramic scaffolds. The composite slurry was formulated by blending PLA with varying contents of HA and BBG powders. The effects of HA and BBG on the rheological behavior and printability of the slurry were analyzed, along with their influences on the scaffold microstructure, wettability, mechanical properties, bioactivity, and degradation rates. The incorporation of ceramics enhanced both the mechanical and biological properties of the scaffolds. These findings advance the current understanding of using DLP 3D printing to fabricate biomimetic polymer–ceramic scaffolds and offer promising insights for advancing current biomaterial technologies and fabrication methods in future biomedical applications.

Bone is the primary component of the mammalian skeletal system, serving key roles in motor function and the protection of internal organs.[1,2] Bone defects are caused by trauma, inflammatory and infectious diseases, congenital malformations, tumor resection, osteoporosis, and bone loss associated with tooth extraction or periodontal disease.[3] Critical bone defects surpass body's natural healing capabilities and require medical intervention for regeneration. Despite advances in treatment outcomes, managing critical bone defects remains a significant challenge in clinical practice. Globally, over 2 million bone grafts take place each year (with approximately 500,000 in the United States), making bone the second most common transplant tissue after blood.[4,5] Autografts, the gold standard for treating critical bone defects, are limited by donor site morbidity, low availability, and prolonged recovery times. Allografts, while readily available, carry risks of immune rejection, infection, and poor integration. Synthetic grafts and bone cement often lack the bioactivity and mechanical robustness for effective bone regeneration, particularly in load-bearing bone.[6–9] BTE has emerged as a promising approach to address critical bone defects by developing scaffolds that mimic bone's extracellular matrix, providing structural support, guiding cell attachment and proliferation, and delivering biochemical cues to enhance osteogenesis.

Besides biocompatibility and bioactivity, BTE scaffolds should be adequately porous to provide vascularization, mechanical strength in the range of surrounding bone, and degradation kinetics aligned with bone regeneration, supporting the fragile healing tissue.[10–12] Traditional methods such as solvent casting, particulate leaching, freeze-drying, gas foaming, and electrospinning have been extensively employed in BTE scaffold fabrication due to their simplicity and scalability.[13,14] However,

these techniques face significant limitations, such as material constraints, restricted customization, limited precision in controlling geometry and porosity, and poor reproducibility.[12,15–17] Additionally, traditional fabrication methods often fall short in replicating the intricate 3D architecture of vascularized bone and the spatial distribution of osteogenic cues essential for successful tissue regeneration.[6–9,18,19]

Recent advances in 3D printing (additive manufacturing) have transformed scaffold fabrication through precise control over geometry, pore architecture, and material composition, allowing for personalized treatments with patient-specific bone scaffolds.[20–23] Various advanced manufacturing methods like vat photopolymerization, powder bed fusion, binder jetting, material extrusion, and directed energy deposition have been employed to fabricate porous scaffolds for BTE.[21,26–29] Among these, vat photopolymerization methods, including SLA and DLP, stand out for their ability to create intricate geometries with high precision and resolution. DLP, in particular, can selectively cure an entire resin layer simultaneously, enabling fast processing, while maintaining excellent surface finish and shape fidelity with micron-level precision. Its compatibility with a broad range of biocompatible materials, including polymers and ceramic composites, establishes DLP as a versatile platform for functional scaffold development.[30,31]

Biomimetic polymer–ceramic scaffolds combine the polymer's flexibility and biodegradability with the ceramic's bioactivity and mechanical strength, mimicking the structure and properties of natural bone.[15] The polymer matrix provides a supportive framework, facilitating cell attachment and proliferation, while the ceramic phase, such as hydroxyapatite (HA), BBG, nanodiamond, clays, etc., enhances osteoinductive and osteoconductive properties, promoting bone mineralization and regeneration.[33–38] Integrating bioactive ceramics such as HA and BBG into photopolymerizable resins enables DLP fabrication of scaffolds with precisely tailored structural and functional properties. This approach, however, requires the slurry to exhibit optimal rheological behavior and curing characteristics for uniform ceramic dispersion, consistent layer curing, and accurate scaffold geometry.[41] Excessive ceramic content can increase viscosity, impeding self-leveling, and potentially causing printing failures. Zhang et al.[42] obtained well-controlled multi-level porous scaffolds by blending calcium phosphate bioceramics with a photosensitive resin composed of polyethylene glycol diacrylate and urethane acrylate. The sintered scaffolds enhanced bone regeneration and osteoinduction in an ectopic preclinical model. In another study, Wang et al.[43] used DLP to fabricate porous BCP bioceramic scaffolds with ~56.3 vol% porosity and a compressive strength of ~20.07 ± 2.09 MPa.

Polylactic acid (PLA) is an FDA-approved[44] biopolymer. It has been widely used in BTE due to its biocompatibility, tunable biodegradability, and favorable mechanical properties.[5,45,46] An effective approach to overcome PLA's hydrophobicity and limited reactivity, which restrict cell adhesion and scaffold integration with surrounding tissues,[18,47,48] is to combine PLA with bioactive materials that can enhance its surface properties, bioactivity, and cellular interactions.[49] HA, the mineral content of natural bone, it is a calcium phosphate-based material with exceptional biocompatibility, bioactivity, and osteoconductive properties, which supports bone ingrowth by forming direct chemical bonds with living tissues.[50] HA contributes to scaffold stiffness and promotes osteointegration. However, low solubility and brittleness limit its standalone use in load-bearing applications.[51] In contrast, BBG is a highly reactive glass that releases various therapeutic ions, including calcium, sodium, magnesium, copper, and zinc, which are essential for promoting bone growth and angiogenesis.[51,52] Ions released from BBG interact with surrounding tissues and biological fluids to form a biologically active calcium phosphate layer on the scaffold surface, promoting strong bonding with the surrounding bone tissue and osteointegration.[53,54] While BBG exhibits excellent bioactivity and biodegradability, its rapid degradation can lead to mechanical instability, resulting in suboptimal bone regeneration.[55–58]

Most research on DLP-printed BTE scaffolds has focused on bioceramics, with few studies exploring the fabrication of polymer–ceramic composite scaffolds.[59,60] The present paper integrates PLA, HA, and BBG for DLP 3D printing, allowing control over scaffold geometry, pore architecture, and material distribution and leveraging the osteoconductive properties of HA, the bioactivity and angiogenic potential of BBG, and the structural versatility of PLA.

In this study, PLA-based scaffolds for bone regeneration, incorporating HA and BBG, were fabricated using DLP 3D printing. We studied the effects of formulation and design on the physical properties of DLP-printed polymer–ceramic scaffolds. The composite slurry was formulated by blending PLA with varying contents of HA and BBG powders. The effects of HA and BBG on the rheological behavior and printability of the slurry were analyzed, along with their influences on the scaffolds' microstructure, wettability, mechanical properties, bioactivity, and degradation rates. The incorporation of ceramics enhanced both the mechanical and biological properties of the scaffolds. These findings advance the current understanding of using

DLP 3D printing to fabricate biomimetic polymer–ceramic scaffolds and offer promising insights for advancing current biomaterial technologies and fabrication methods in future biomedical applications.

2. Materials and methods

2.1. Materials

The commercial PLA photocurable resin composition with 2–3% methacrylate monomers (X15 Transparent, Uniformation, Shenzhen, China), HA powder (Sigma-Aldrich, MO, USA), and BBG powder (ETS Wound Care, MO, USA) were used as the polymer matrix and ceramic fillers, correspondingly. The BBG used in this study is 1605 borate glass composed of 51.6 wt.% B_2O_3, 20 wt.% CaO, 6 wt.% Na_2O, 5 wt.% MgO, 4 wt.% P_2O_5, 12 wt.% K_2O, 1 wt.% ZnO, and 0.4 wt.% CuO. Isopropyl alcohol was used to dissolve and remove the uncured resin composition from printed parts. Dulbecco's Modified Eagles Medium (DMEM), phosphate-buffered saline (PBS), fetal bovine serum (FBS), penicillin/streptomycin (pen/strep), MTT, and trypsin/EDTA were purchased from Sigma-Aldrich.

The particle size distributions of the HA and BBG were measured by a Microtrac S3500 tri-laser diffraction particle analyzer (Microtrac Inc., PA, USA). Approximately, 100 mg of each powder was suspended in 10 mL deionized water to prevent agglomeration. Particle morphology was observed by scanning electron microscopy using Helios 5 Hydra DualBeam SEM (Thermo Fisher Scientific, MA, USA) at 5 kV acceleration voltage and 8 mm working distance under a high vacuum. Figure 1 shows the particle size distribution and SEM micrographs of HA and BBG. The D50 values for HA and BBG are 14.27 and 9.99 μm, respectively. BBG particles showed a smoother and more round morphology with a unimodal particle size distribution, while HA particles exhibited sharper edges and a bimodal distribution.

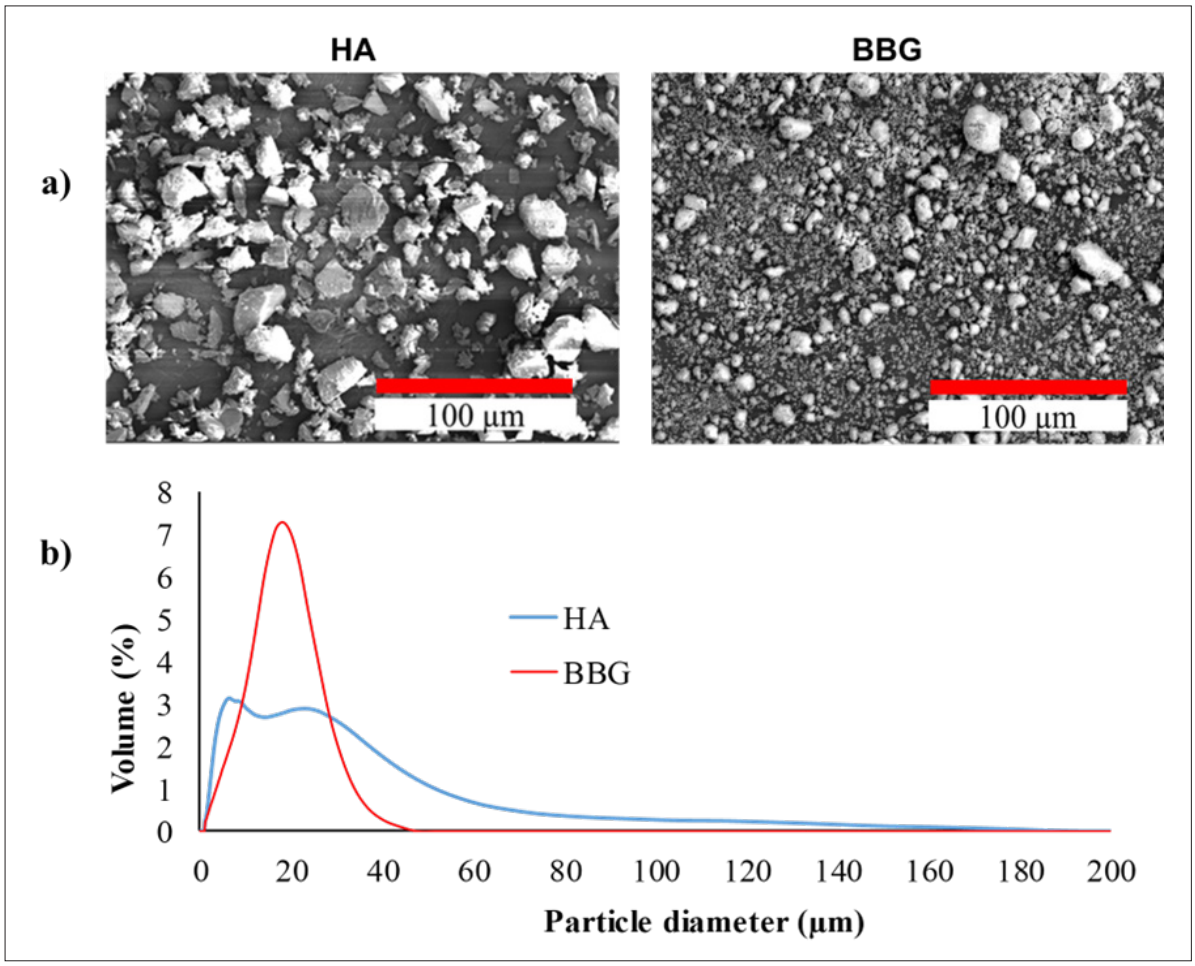

Figure 1. SEM micrographs (a) and particle size distribution (b) of HA and BBG samples. Abbreviations: BBG, bioactive borate glass; HA, hydroxyapatite; SEM, scanning electron microscopy.

2.2. Preparation of slurry suspension

UV-curable suspensions were prepared by blending 0–20% w/v of HA and BBG powders with the commercial photocurable PLA resin composition to obtain composite slurries, as described in our previous work.[61] The composition of the polymer–ceramic slurries and the corresponding sample names adopted in this research are detailed in Table 1.

2.3. 3D printing of scaffolds

The porous scaffolds were designed in SolidWorks software (Dassault Systems Solidworks Corp., MA, USA) with small (S), medium (M), and large (L) pore sizes of 500, 650, and 800 µm, respectively. Anycubic Photon Workshop software was used to slice the 3D models and generate G-code for printing. Scaffolds were fabricated using a commercial DLP 3D printer (Anycubic Photon 5M, Shenzhen, China) equipped with a UV light projector (wavelength 405 nm). Figure 2 depicts a schematic of DLP printing of polymer–ceramic scaffolds. UV light from LED source positioned below the vat reaches the sample through a transparent window to solidify resin layer by layer. Scaffolds were printed with a layer thickness of 50 µm, exposure time of 2.7 s, and 3-s off time. After printing, they were rinsed with isopropyl alcohol, and residual uncured slurry was removed from the pores using airflow. To enhance the overall strength, the scaffolds were subsequently exposed to UV light for 10 min.

2.4. Characterization

The rheological behavior of the slurries was assessed by a rotational rheometer Kinexus Ultra+ (Malvern Panalytical Ltd., Malvern, UK). All measurements were carried out at room temperature (24 °C), with the shear rate ramping up from 0 to 100 s^{-1}. The pore sizes of the small, medium, and large scaffolds were measured using ImageJ software on light microscope images.

The scaffold porosity was calculated using Archimedes principle, following the ASTM F2450-10 standard.[62] The

Table 1. Composition of slurries for DLP printing

Slurry sample	PLA resin composition (mL)	HA (g)	BBG (g)
PLA	100	0	0
PLA-10HA	100	10	0
PLA-15HA	100	15	0
PLA-20HA	100	20	0
PLA-10HA-10BBG	100	10	10
PLA-10BBG	100	0	10
PLA-20BBG	100	0	20

Abbreviations: BBG, bioactive borate glass; DLP, digital light processing; HA, hydroxyapatite; PLA, polylactic acid.

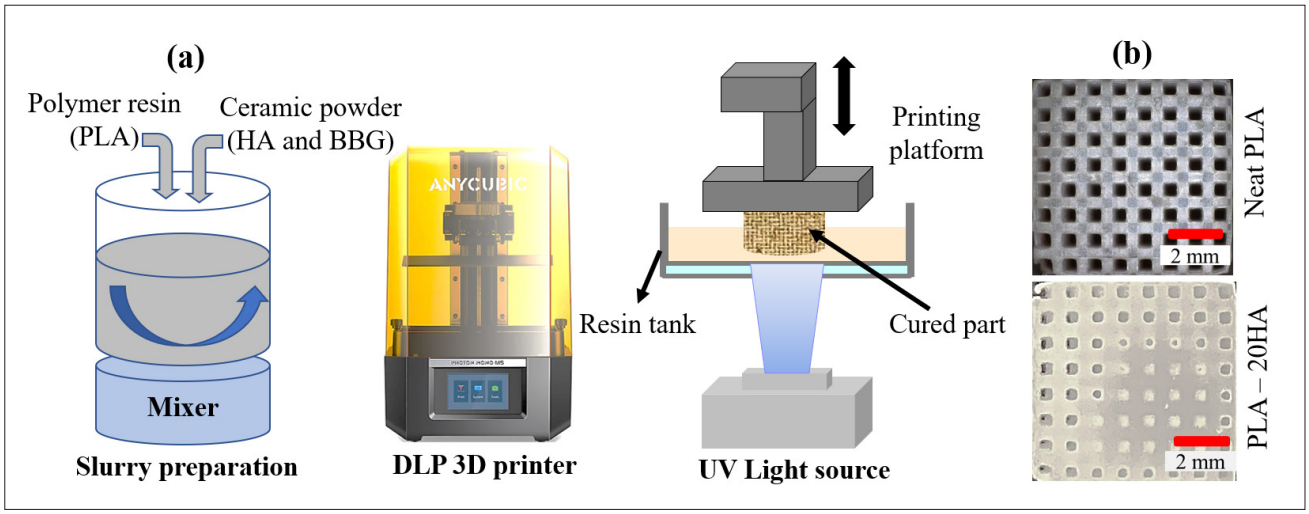

Figure 2. Schematic of DLP 3D printing of polymer–ceramic scaffolds (a) and sample printed parts (b). Abbreviations: BBG, bioactive borate glass; DLP, digital light processing; HA, hydroxyapatite; PLA, polylactic acid.

scaffold apparent density (ρ_a), pore volume (Vp), and porosity (P) were calculated using **Equations I–III**:

$$\rho_a = \frac{W_{dry} \times \rho_e}{W_{dry} - W_{wet}} \quad \text{(I)}$$

$$V_p = V_a - \frac{W_{dry}}{g \times \rho_a} \quad \text{(II)}$$

$$P(\%) = \frac{V_p}{V_a} \times 100 \quad \text{(III)}$$

where ρ_e is the density of ethanol, g is the standard acceleration of free fall (9.8 m/s^2), and W_{dry} and W_{wet} are the sample weight before and after immersing in ethanol, respectively. V_a is the apparent volume of the sample, calculated using its external dimensions.

The contact angle between the scaffold and a droplet of water was measured using a goniometer. For each experiment, a 5 µL water droplet was applied to the scaffold surface and an optical image was captured with a microscope to assess the contact angle. The surface roughness (R) of the scaffolds was analyzed using a 3D digital microscope KH-8700 (Hirox Co Ltd., Tokyo, Japan).

X-ray diffraction (XRD) was conducted using a Rigaku Smartlab at a scanning rate of 10°/min within 2θ values from 20° to 60° to analyze the scaffold's phase composition. The Fourier transform infrared (FTIR) spectra were recorded with a Nicolet iS50 spectrophotometer (Thermo Fisher Scientific), outfitted with a mid-IR range (4000–400 cm^{-1}) diamond crystal cell for attenuated total reflection. Scaffolds were placed over the crystal on the splitter area and spectra acquired at a 4 cm^{-1} resolution, 32 scans per spectrum with a data interval of 0.482 cm^{-1}. Spectral analysis was performed using the OMNIC software version 9.2.41 (Thermo Fisher Scientific).

Thermogravimetric analysis (TGA) was conducted using a TGA/DSC 3+ instrument (Mettler Toledo, Schwerzenbach, Switzerland) to determine the actual ceramic content in the printed scaffolds. Due to resin–ceramic interactions and potential ceramic sedimentation during 3D printing, the ceramic content in the printed parts may differ from that in the original slurry. The TGA was performed in two stages: an initial isothermal segment at 150°C in argon atmosphere at a flow rate of 100 mL/min for 60 min to remove volatiles including adsorbed water, followed by a dynamic segment with a temperature rise from 150 to 700°C at 5°C/min in oxygen flow (100 mL/min) for complete burning of organic matter, leaving only the ceramic residue.

2.5. Mechanical properties

Mechanical properties of the 3D-printed scaffolds were evaluated by compressive strength tests, using an MTS Landmark materials testing system with a 250 kN load cell. The compressive strength was determined from stress–strain curves recorded at a loading speed of 1 mm/min at room temperature. The average compressive strength and standard deviation were calculated from at least five measurements. To determine the elastic modulus of the scaffolds, stress–strain curves were obtained from compressive testing results. The modulus was calculated from the initial linear region of the stress–strain curves, representing elastic behavior.

2.6. Bioactivity and biodegradation

The bioactivity of the scaffolds was evaluated by soaking the samples in simulated body fluid (SBF) prepared according to Kokubo and Takadama[63] at 37°C. The 3D-printed scaffolds, with approximate dimensions of 7.8 × 7.8 × 6.1 mm^3, were weighed, thoroughly rinsed with ethanol and deionized water, and air-dried at room temperature. Each scaffold was then individually soaked in 5 mL of SBF, maintaining a mass-to-liquid ratio of approximately 50 mg/mL, for 4 weeks. After the incubation period, the scaffolds were carefully removed, air-dried at room temperature, and stored at 4°C.

Surface morphology of the scaffolds was examined using Helios 5 Hydra DualBeam scanning electron microscope (Thermo Fisher Scientific) at an accelerating voltage of 10 kV and a working distance of 5.7 mm. The samples were coated with gold using Denton Desk V coater prior to imaging.

The elemental composition of the scaffolds was mapped using energy-dispersive X-ray spectroscopy (EDS) to study the deposition and distribution of calcium phosphate layers, formed on the scaffolds surface after immersing in SBF. EDS mapping and point analyses were conducted to quantify key elements such as calcium, phosphorus, and oxygen.

The degradation rate of the 3D-printed samples was measured after immersion in SBF at 37 °C. Approximately 500 mg of each sample was weighed and placed in 6 mL of SBF in 12-well plates, with three replications. At predetermined timepoints, the samples were carefully removed, dried at room temperature, and weighed. The weight changes were monitored over a 12-week period using **Equation IV**:

$$\text{Weight loss}(\%) = \frac{W_0 - W_t}{W_0} \times 100 \quad \text{(IV)}$$

where W_0 is the initial dry weight, and W_t is the dry weight at a given timepoint during immersion in SBF.

2.7. *In vitro* biocompatibility

The MTT assay was employed to evaluate the viability of human osteosarcoma cells (MG63, ATCC, USA) in contact with the 3D-printed scaffolds. In accordance with ISO-10993 standard, sample extracts were used for indirect cell viability assessment. Extracts were collected and filtered after 7 days of scaffold immersion in DMEM with three replicates. DMEM culture media served as blank control. Initially, MG63 cells were cultured in 100 µL of DMEM media supplemented with 10% FBS and 1% pen/strep at a density of 10,000 cells per well and incubated at 37 °C in 5% CO_2. After 24 h, the initial media were replaced with 90 µL of sample extract fortified with 9% FBS and 1% pen/strep. Following another 24 h, the media were replaced with 100 µL of 0.5 M MTT solution. After 4 h of incubation, the MTT solution was replaced with 100 µL of isopropanol to dissolve formazan crystals. Finally, the optical density (OD) of formazan was measured at 545 nm using an ELISA reader Stat Fax 2100 (Awareness Technology, Inc., FL, USA).

2.8. Statistical analysis

All experiments in this study were conducted with a minimum of three replicates per sample for each test. Data are presented as mean ± standard deviation (SD). Statistical differences among groups were evaluated using one-way analysis of variance (ANOVA), which assesses overall group differences and identifies significant variations between group means. $p < 0.05$ was considered statistically significant. All statistical analyses were performed using Microsoft Excel.

3. Results and discussion

The design and fabrication of effective BTE scaffolds require careful consideration of material characteristics, structural geometry, biological functionality, and manufacturing feasibility. The overall performance of the scaffold is shaped by both the intrinsic properties of its components and their interactions during fabrication and under physiological conditions. These interactions govern critical factors such as mechanical strength, bioactivity, degradation behavior, and cellular compatibility, all of which must be harmonized to achieve functional tissue regeneration.

3.1. Rheological behavior and structural analysis of slurries

The rheological behavior of PLA-based composite slurries significantly influences their printability, layer resolution, dimensional accuracy, and scaffold integrity. Figure 3 shows how slurry composition affects viscosity and shear rate. The as-received commercial PLA resin composition demonstrated near-Newtonian behavior, maintaining a stable viscosity of approximately 361 mPa·s across varying shear rates. This behavior, characteristic of low-viscosity slurries, results from minimal interparticle interactions, enabling smooth flow and self-leveling during the DLP printing process. Incorporating HA into PLA resin markedly increased viscosity, particularly as HA concentration rose from 10 to 20 wt.%. The shear-thinning behavior, where viscosity decreases with increasing shear rate, is evident in the declining viscosity at higher shear rates, reflecting interparticle interactions and irregular morphology of HA particles, which impede the flow. PLA-20HA exhibited the highest viscosity, which can induce a jamming effect due to irregular morphology, sharp edges, and large size of HA particles (Figure 1), thus restricting the flow within the polymer matrix.[43,64] At low shear rates, this jamming effect dominates, leading to viscosities approaching 60,000 mPa·s for PLA-20HA, which may present potential challenges for printability. Similar observations by Xu et al.[65] reported HA-based slurries with viscosities 40,000–70,000 mPa·s requiring precise shear-thinning characteristics for effective layer deposition. Beyond this range, severe jamming and sedimentation further impair printability. Consequently, PLA-15HA and PLA-20HA were deemed unprintable due to excessive viscosity and were excluded from further scaffold experiments.

Conversely, BBG had a minimal effect on viscosity, with PLA-10BBG and PLA-20BBG slurries maintaining values below 500 mPa·s. This behavior can be explained by several mechanisms. First, the spherical morphology and smaller particle size of BBG reduce interparticle friction and clustering, thereby facilitating smoother flow compared to the irregular, angular particles of HA. Additionally, unlike HA, which is chemically stable, BBG's higher ionic activity, attributed to mobile ions such as Ca^{2+}, Na^{+}, and B^{3+}, enhances surface reactivity in the slurry. The electrostatic interactions between BBG ions and the charged functional groups of the resin reduced the interparticle aggregation and enabled better particle dispersion within the slurry. On a molecular level, the carbonyl-oxygen linkage (COO) within the ester functional group in methacrylate monomers within the PLA resin, are capable of weakly interacting with BBG ions through dipole–ion interactions, which, unlike HA, improves particle dispersion and prevents aggregation. Interestingly, the PLA-10HA-10BBG slurry showed a viscosity profile similar to PLA-10HA, suggesting that HA dominates the viscosity profile in the hybrid formulation. The irregular morphology and high surface area of HA are likely to

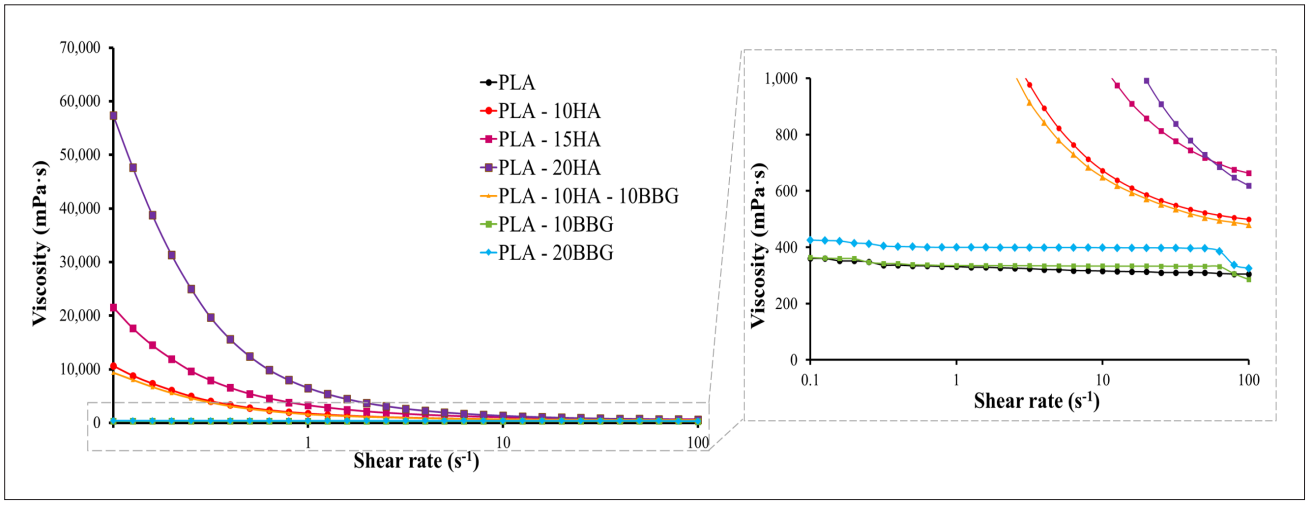

Figure 3. Viscosity versus shear rate of PLA-based composite slurries. Abbreviations: BBG, bioactive borate glass; HA, hydroxyapatite; PLA, polylactic acid.

contribute to its dominant influence, overshadowing the fluidity-enhancing effects of BBG.

The structural composition and crystalline phases of the 3D-printed PLA-based scaffolds were analyzed using X-ray diffraction (XRD), as shown in Figure 4. The XRD patterns of PLA, PLA-10BBG, and PLA-20BBG scaffolds lack sharp characteristic peaks, confirming their predominantly amorphous structure.[55,66] The broad peaks at 2θ = 8.98° and 19.25° reflect semicrystalline nature of PLA, suggesting a mixture of amorphous and crystalline regions at room temperature.[67] These broad peaks signify partial crystallization of the PLA molecular chains due to the rapid polymerization during the DLP printing process, which limits extended crystalline domain formation.

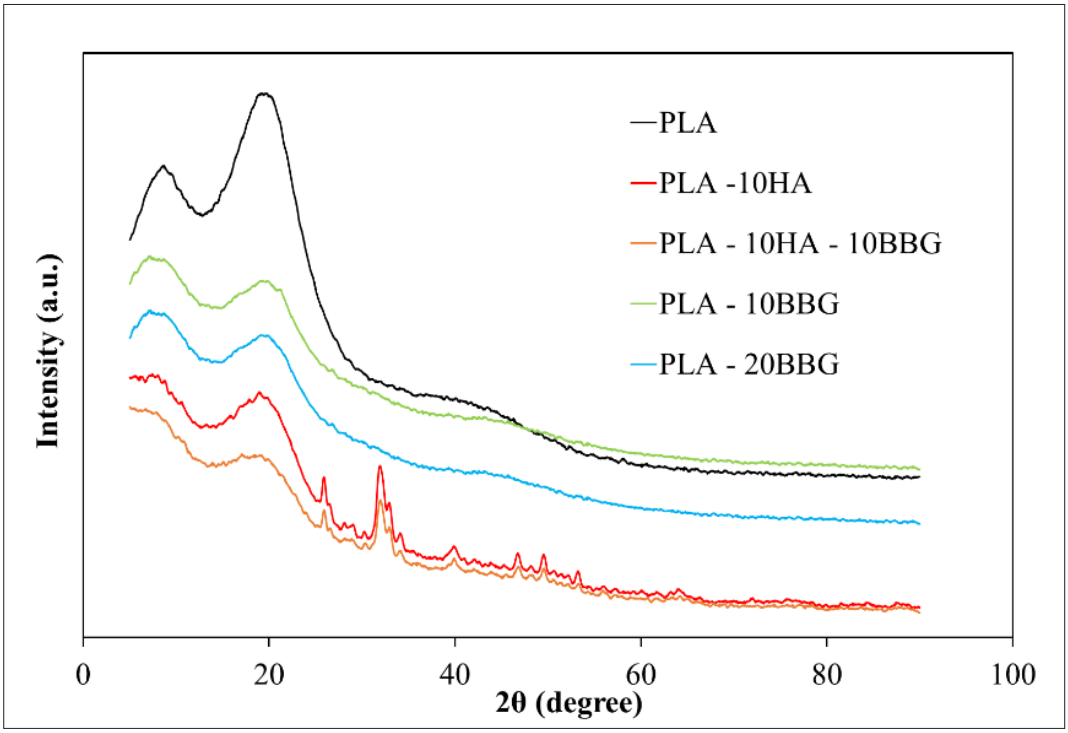

Figure 4. X-ray diffraction (XRD) pattern of neat PLA, PLA-10HA, PLA-10HA-10BBG, PLA-10BBG, and PLA-20BBG scaffolds. Abbreviations: BBG, bioactive borate glass; HA, hydroxyapatite; PLA: Polylactic acid.

After incorporating BBG, the PLA's semicrystalline characteristic peak at 19.25° exhibited a slight shift to 20.08°, as observed in PLA-10BBG and PLA-20BBG, suggesting a reduction in lattice spacing within the polymer matrix, possibly caused by enhanced interactions between the BBG particles and the PLA chains. These interactions could stem from the presence of mobile ions (e.g., Ca^{2+}, Na^{+}, and B^{3+}) in BBG, which interact with the polar ester groups of PLA and carbonyl-oxygen linkage in methacrylate groups via ion–dipole interactions. The interactions disrupt the regularity of the PLA chains, promoting amorphization and hindering crystallization. The increased amorphization also leads to broader and less defined peaks in PLA-20BBG, confirming BBG's role in disrupting crystalline domain formation. However, excessive ceramic particle loading, as in PLA-20BBG, may also introduce structural heterogeneity, for example, agglomerates, potentially affecting the scaffold's mechanical strength and integrity.

In contrast, the XRD patterns of HA-incorporated PLA scaffolds (PLA-10HA and PLA-10HA-10BBG scaffolds) exhibit distinct crystalline peaks that align with the reference pattern of HA (JCPDS #09-0432). No other characteristic peaks besides those of HA and PLA were observed, consistent with sample composition. HA characteristic peaks at 2θ = 25.9°, 31.9°, 33.0°, 46.7°, and 49.5° correspond to its (002), (211), (300), (222), and (213) planes, indicating that HA retains its crystalline structure during the composite fabrication process. The higher intensity of these peaks in PLA-10HA scaffolds compared to PLA-10HA-10BBG suggests that HA dominates the crystalline phases in PLA-10HA scaffolds. The slightly lower intensity of HA characteristics peaks in PLA-10HA-10BBG scaffolds can be attributed to the amorphous nature of BBG, which dilutes the content of HA and enhances diffuse scattering during the XRD measurements.

The chemical structure of various PLA-based composite scaffolds was analyzed using FTIR spectroscopy, as shown in Figure 5. In PLA scaffolds, the peaks observed between 3000 and 2850 cm^{-1} correspond to C–H stretching in =CH– and $–CH_3$ groups of the polymer backbone.[49] The strong absorption peak at 1721 cm^{-1} is attributed to the carbonyl (C=O) stretching in ester functional groups that connect the repeating lactic acid units in the PLA polymer chain.[68] The peak at 1406 cm^{-1} arises from C–H bending vibrations in $–CH_3$ groups.[69,70] The peaks at 1191 and 1080 cm^{-1} correspond to C–O stretching in the ester

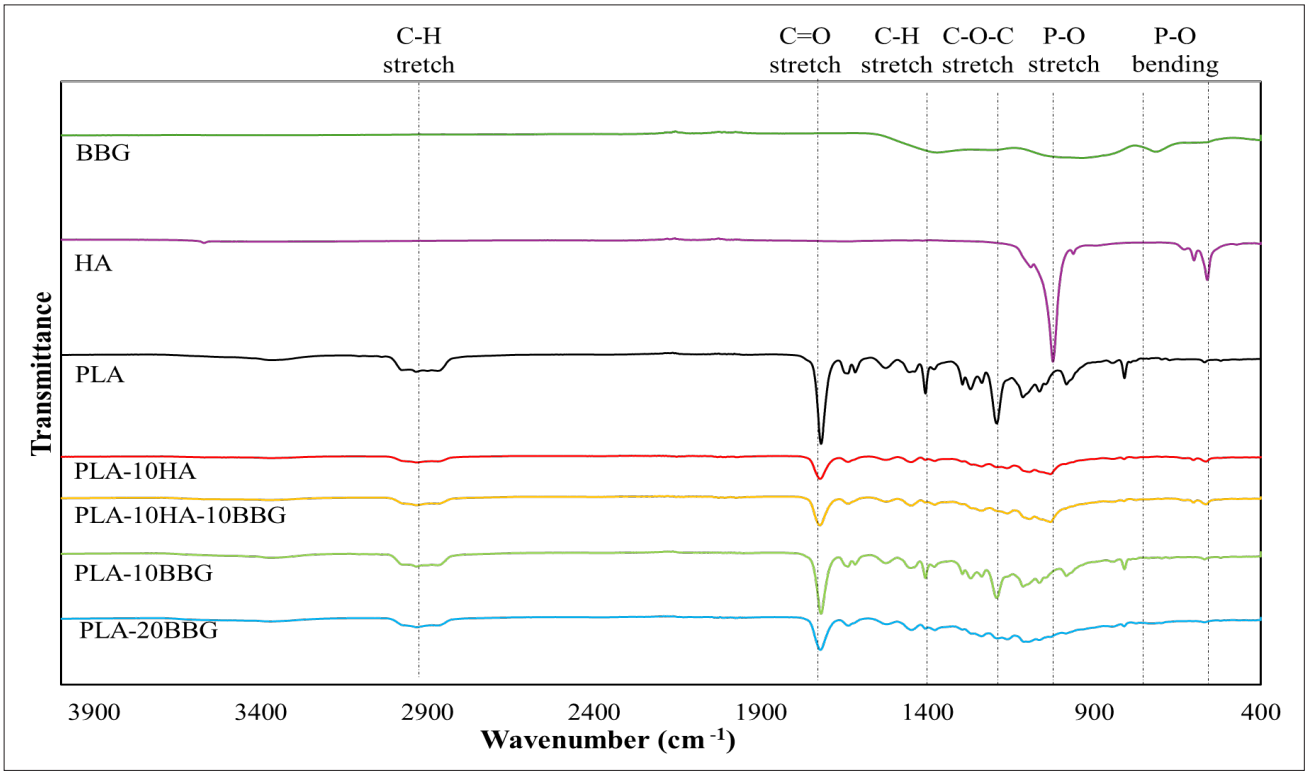

Figure 5. FTIR spectra of PLA, PLA-10HA, PLA-10HA-10BBG, PLA-10BBG, and PLA-20BBG scaffolds. Abbreviations: BBG, bioactive borate glass; FTIR, Fourier transform infrared; HA, hydroxyapatite; PLA, polylactic acid.

groups.[71] As expected, these peaks are consistently observed across all of the PLA-based scaffolds.

The FTIR spectrum of neat HA shows distinct peaks corresponding to its phosphate groups. A prominent peak at 1030 cm^{-1} is associated with the asymmetric stretching vibrations of phosphates (PO_4^{3-}), while bending vibrations appear at 565 cm^{-1}.[72] As expected, the addition of HA to PLA reduces the overall intensity of the characteristic peaks of PLA. The 1030 cm^{-1} phosphate peak becomes less intense and broader, possibly due to interactions between HA and the PLA matrix. Additionally, carbonyl oxygen in the PLA's methacrylate groups may weakly interact with HA through hydrogen bonding, increasing the width and reducing intensity of the C=O peak.

The FTIR spectrum of neat BBG exhibits broad, low-intensity peaks between 1400 and 600 cm^{-1}, indicative of its amorphous nature. These broad features correspond to B–O stretching vibrations in boron–oxygen linkages at approximately 1350–1250 cm^{-1} and the peaks appearing in the 1000–600 cm^{-1} range, associated with metal oxides, such as Ca–O, Mn–O, Cu–O, and Zn–O.[34] However, these BBG-related peaks are not prominent in the PLA-10BBG, PLA-20BBG scaffolds, as the BBG particles are well-dispersed within the PLA matrix. The interactions between PLA chains and BBG likely involve dipole–ion interactions between BBG's mobile ions (e.g., Ca^{2+}, Na^{+}) and PLA's carbonyl (C=O) groups. Such interactions disrupt the regularity of PLA chains, as evidenced by the slight shifts and broadening of the carbonyl peak at 1721 cm^{-1}. The spectra of PLA-10HA-10BBG scaffolds display overlapping features of HA and BBG. The 1030 cm^{-1} phosphate peak from HA is less intense, and BBG's peaks contribute to the overall spectral profile but appear less distinct.

The ceramic content of 3D-printed samples may vary from the original slurry composition due to particle precipitation, non-uniform distribution, and other factors during the DLP process. TGA analysis was performed to measure the actual ceramic content in the printed scaffolds, as depicted in Figure 6. According to the literature, PLA has a glass transition temperature (T_g) of approximately 53–55 °C and primarily decomposes between 300 and 500 °C.[73–75] The melting point of neat PLA typically ranges between 170 and 240 °C, depending on its crystallinity and molecular weight. PLA with a higher degree of crystallinity exhibits higher melting point.[76] Amorphous PLA may exhibit a lower melting point or may not show a distinct melting peak, instead transitioning directly into the viscous state upon heating (Figure 6b). Addition of HA to PLA increased its crystallinity and shifted the melting temperature to 216 °C, thus broadening the temperature window of the scaffold's solid state. All scaffold samples exhibited a two-step weight loss (Figure 6a) during their thermal degradation in oxygen atmosphere. First, a minor weight loss between 150 and 270 °C corresponds to evaporation of residual moisture and other volatiles, followed by major weight loss associated with burning off of the combustible content of the sample between 270 and 500 °C. Incorporating HA and BBG alters the weight loss profile. PLA-10HA scaffolds degrade at a slightly lower temperature (maximum degradation at ~478.3 °C), which may be due to the interfacial stress between the PLA matrix and the rigid HA particles, leading to microstructural defects. Incorporation of BBG into scaffolds has a smaller

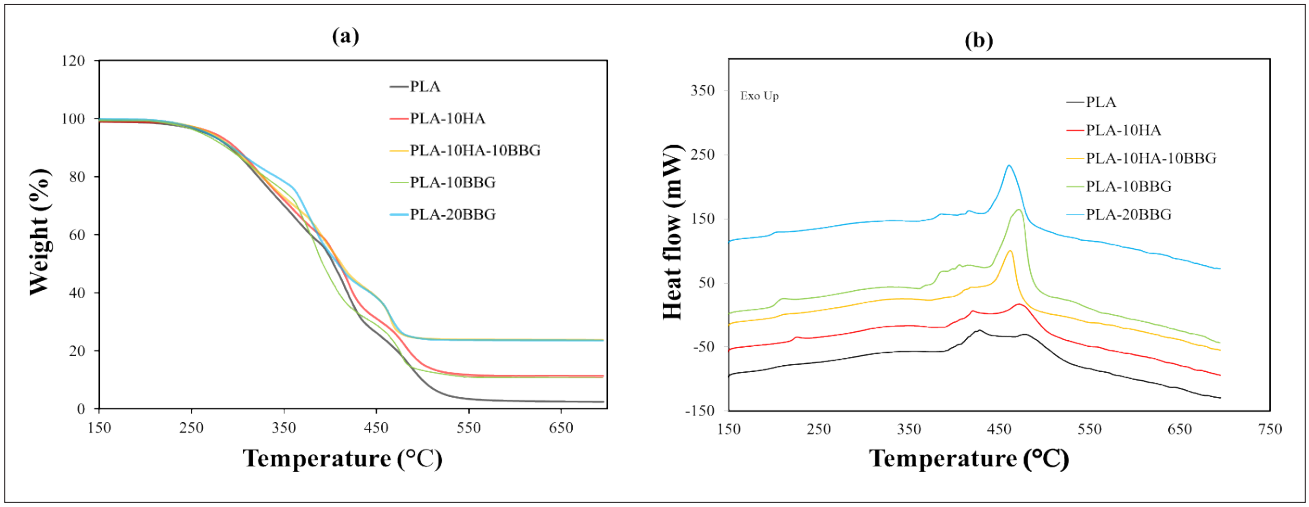

Figure 6. Thermal analysis of the neat PLA, PLA-10HA, PLA-10HA-10BBG, PLA-10BBG and PLA-20BBG: (a) TGA and (b) DSC. Abbreviations: BBG, bioactive borate glass; DSC, differential scanning calorimetry; HA, hydroxyapatite; PLA, polylactic acid; TGA, thermogravimetric analysis.

effect on their melting temperature, with PLA-10BBG and PLA-20BBG showing melting points of approximately 193.9 and 196.3°C, respectively. Exothermic peaks corresponding to the maximum burning rates were observed at 481.9°C for PLA, 478.3°C for PLA-10HA, 464.4°C for PLA-10HA-10BBG, 469°C for PLA-10BBG, and 463.3°C for PLA-20BBG. Combustion is complete at 619°C for PLA, 554.2°C for PLA-10HA, 536.9°C for PLA-10HA-10BBG, 558.6°C for PLA-10BBG, and 575.8°C for PLA-20BBG. All scaffolds showed that the incorporation of ceramics to PLA resulted in a decrease in both the temperature of the maximum decomposition and the overall decomposition temperature. This effect can be attributed to the interfacial interactions between HA and PLA, as well as to increased destabilization of the PLA structural framework within the composites.[77]

The residual mass after thermal decomposition of neat PLA is approximately 2.4%, likely due to inorganic additives present in the commercial PLA resin.[78] The density of PLA is 1.1 g/mL, leading to an actual content of 8.3% for scaffolds with 10 w/v% ceramic addition and 15.4% for those with 20 w/v% ceramic addition. PLA-10HA had a residual mass of about 8.9%, slightly higher than the amount of ceramic added to the resin.

3.2. Scaffold microstructure and porosity

Porosity is a key property of BTE scaffolds, directly influencing their mechanical performance and degradation kinetics, cell attachment, cell migration, vascularization, nutrient and oxygen transport, and new tissue growth. Pore sizes commonly used in BTE scaffolds vary between 100 and 900 μm. Osteoblasts (10–50 μm in size) prefer pore sizes greater than 300 μm as this enables infiltration of biomolecules and transport of nutrients and wastes.[79] Figure 7 presents optical images of 3D-printed scaffolds with different compositions, highlighting the effect of HA and BBG on modulation of structural attributes during DLP fabrication. The average porosity and pore size (side length) of the 3D-printed scaffolds are provided in Table 2. The data reveal variations among the scaffolds, reflecting the effects of material composition on resin curing dynamics and light scattering during the photopolymerization process. PLA-10HA scaffolds, which have the highest viscosity among our printed samples, exhibited the largest discrepancy in porosity and pore size compared to the intended values. The higher viscosity of PLA-10HA slurries reduces flowability, resulting in lower accuracy compared to the intended pore geometry. Additionally, the irregular particle morphology as well as high refractive index and light-scattering effects of HA lead

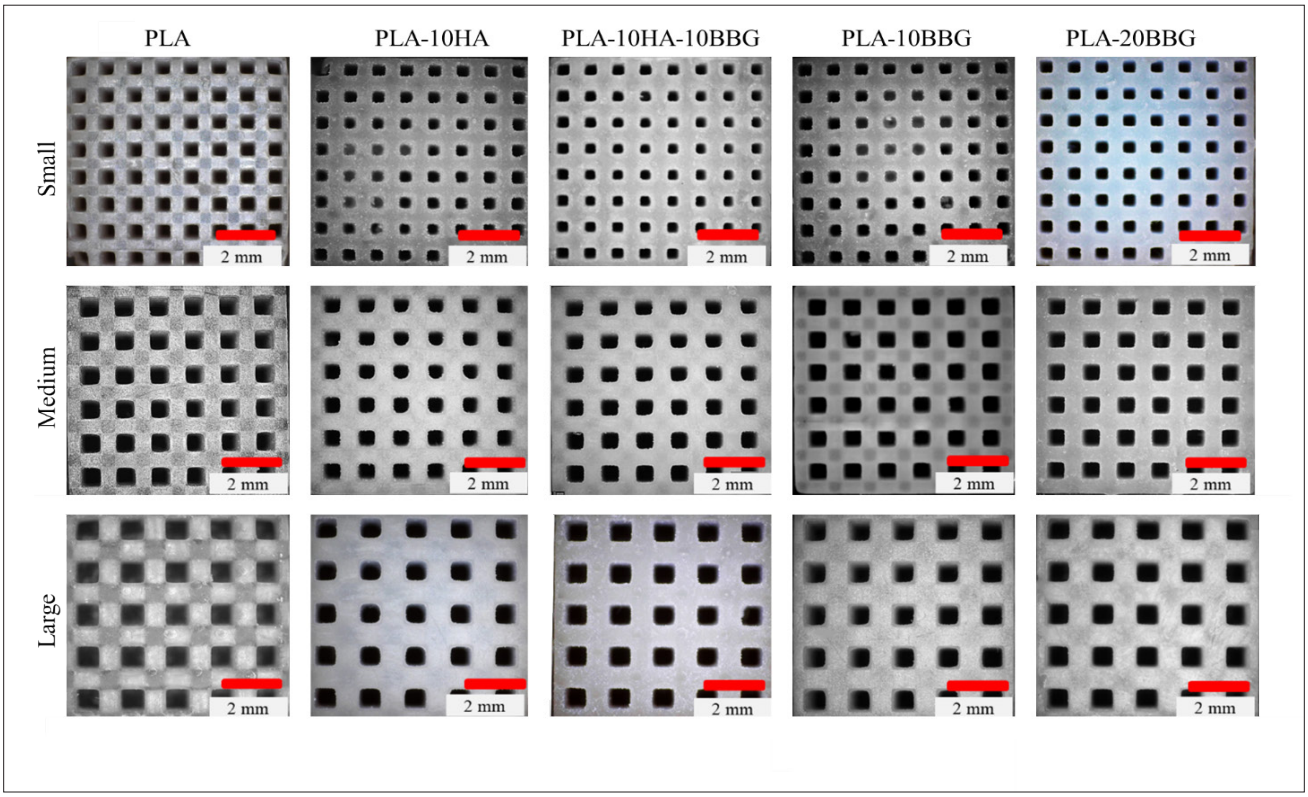

Figure 7. Optical micrographs of small (S), medium (M), and large (L) pores in DLP-fabricated PLA, PLA-10HA, PLA-10HA-10BBG, PLA-10BBG, and PLA-20BBG scaffolds. Abbreviations: BBG, bioactive borate glass; DLP, digital light processing; HA, hydroxyapatite; PLA, polylactic acid.

Table 2. The porosity and pore size of the 3D-printed scaffolds

Scaffolds	Porosity (%)			Pore size (μm)		
	S	M	L	S	M	L
Intended	50	50	50	500	670	800
PLA	52.7 ± 2.1	51.6 ± 1.4	52.8 ± 2.7	531.8 ± 11.6	676.1 ± 11.8	844.7 ± 19.8
Deviation (%)	5.4	3.2	5.6	6.36	0.91	5.59
PLA-10HA	46.3 ± 5.1	48.8 ± 4.2	49.3 ± 2.7	458.6 ± 14.9	571.3 ± 26.5	722 ± 21.3
Deviation (%)	−7.4	−2.4	−1.4	−8.28	−14.73	−9.75
PLA-10HA-10BBG	48.7 ± 5.7	49.2 ± 2.6	49.9 ± 2.3	464.7 ± 16.7	612.9 ± 24.7	766.6 ± 23.5
Deviation (%)	−2.6	−1.6	−0.2	−7.06	−8.52	−4.18
PLA-10BBG	51.1 ± 1.3	50.7 ± 2.1	51.3 ± 1.5	520.4 ± 15.6	659.8 ± 14.4	820.4 ± 24.2
Deviation (%)	2.2	1.4	2.6	4.08	-1.52	2.55
PLA-20BBG	49.1 ± 3.4	48.9 ± 2.8	52.1 ± 2.5	489.2 ± 19.8	622.6 ± 25.1	768.4 ± 27.2
Deviation (%)	−1.8	−2.2	4.2	−2.16	−7.07	−3.95

to uneven curing, partial overcuring, and overall structural distortion. The difference in refractive index between the ceramic particles and the photosensitive monomer has a negative effect on the curing ability and printability in the DLP process.[80] This mismatch can lead to inefficient transmission and scattering of light, resulting in incomplete polymerization, compromising structural integrity of the printed scaffolds.[80,81]

PLA and PLA-10BBG scaffolds exhibited pore sizes mostly larger than the intended designs, while PLA-10HA, PLA-10HA-10BBG, and PLA-20BBG exhibited pore sizes mostly smaller than the intended designs. Although PLA and PLA-10BBG scaffolds show similar results in terms of increased pore size, the mechanisms are different. In PLA scaffolds, the increase in pore size can be due to shrinkage-driven pore expansion during resin curing and post-curing processes. Neat PLA resin lacks ceramic particles that could hinder polymerization or scatter light, resulting in a more uniform and consistent curing process. During photopolymerization, the PLA resin undergoes volumetric shrinkage as the liquid monomer converts into a solid polymer network. The shrinkage produces tension within the scaffold structure, which may expand the pore walls outward due to the absence of reinforcing ceramic fillers.[82,83] Consequently, the pore size increases slightly compared to the intended design. Additionally, the lack of ceramic particles blocking the UV light during photopolymerization results in more uniform curing. For PLA-10BBG, unlike PLA-10HA, BBG's smooth particle morphology and reduced light scattering (due to lower refractive index compared to HA) promote more uniform polymerization, reducing structural collapse or pore shrinkage. Thus, PLA-10BBG scaffolds have larger porosities and pore sizes than PLA-10HA scaffolds. PLA-20BBG produced scaffolds with smaller porosities and pore sizes than PLA-10BBG. This can be attributed to the higher concentration of BBG, which may cause more particle sedimentation during the printing process, leading to less uniform distribution of ceramic particles within the PLA resin. The higher ceramic content in PLA-20BBG scaffolds could also cause higher degree of light scattering, particularly at larger layer thicknesses, resulting in undercured regions or partial collapse of the pore walls. Furthermore, higher particle loading increases the overall solid content that may restrict free volume within the pores, leading to smaller pore sizes.

Figure 8 depicts the SEM images and corresponding surface roughness (R) of the scaffolds. The R values were obtained from 3D digital light microscopy as the average deviations from the mean surface level. Larger xcv indicates a rougher surface with greater irregularities, while smaller R indicates a smoother surface. Optimal surface roughness can significantly enhance bone-to-implant contact and cell attachment, making it a critical factor in scaffold design.[78] Studies have shown that the osteoinductive capacity of scaffolds strongly correlates with their roughness: rough surfaces promote biomineralization and interaction with mesenchymal stem cells.[37,38,84,85] PLA scaffolds have the smoothest surface with the lowest R values, which tend to increase upon adding HA and BBG. The smooth surface in PLA scaffolds, with minimal irregularities, results from uniform curing, consistent with neat PLA's low viscosity, and the absence of ceramic particles. A significantly rougher texture is evident in PLA-10HA scaffolds, with visible agglomerates of HA on the scaffold surface. The irregular, angular morphology of HA particles (Figure 1), coupled with their chemical inertness, and lack of ionic interactions results in poor dispersion within the polymer matrix. PLA-

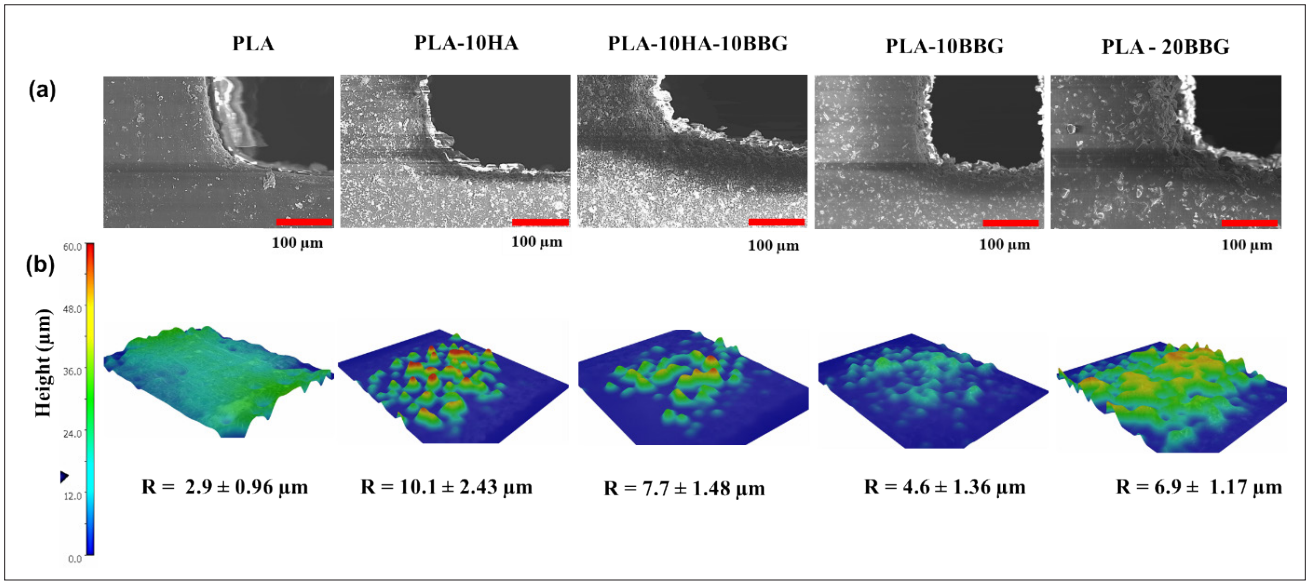

Figure 8. SEM images and surface roughness of the PLA-based scaffolds. Abbreviations: PLA, polylactic acid; SEM, scanning electron microscopy.

10HA-10BBG scaffolds exhibit mixed morphology where ceramic particles appear partially embedded in the matrix and the roughness is less pronounced compared to PLA-10HA. The surface of PLA-10BBG is smoother compared to the other ceramic–polymer scaffolds, but still slightly rougher than PLA scaffolds. The smoother morphology of PLA-10BBG scaffolds is likely due to the smaller particle size and rounded shape of BBG, which facilitates particle dispersion, while in PLA-20BBG scaffolds the surface shows an intermediate roughness, slightly higher than PLA-10BBG but still smoother than PLA-10HA. With higher BBG content, the likelihood of particle clustering and sedimentation increases. While BBG particles are smaller and smoother than HA, higher BBG loading reduces the free volume within the resin, causing uneven dispersion.

3.3. Mechanical properties

The compressive strength of non-porous and porous PLA-based composite scaffolds demonstrates that the material composition and pore architecture influence its mechanical properties. The compressive strength of non-porous PLA is 48.9 ± 4.89 MPa, the lowest value among the tested compositions as shown in Figure 9a. The incorporation of HA and BBG enhances the strength of the composite, indicating that these fillers augment the load-bearing capacity of the material through their inherent rigidity and interactions with the PLA matrix.[86] Regardless of the pore design, PLA-10HA scaffolds demonstrate the highest compressive strength among all samples, indicating that the incorporation of HA significantly enhances the mechanical properties of the composite. The compressive strength of nonporous PLA-10HA scaffolds, measured at 64.5 ± 3.6 MPa, reflects the ability of the HA particles as a physical filler to distribute and bear applied mechanical load. The compressive strength of porous PLA-10HA scaffolds decreased substantially to 10.9 ± 1.2 MPa, an ~85% reduction compared to their nonporous counterparts. As expected, all porous samples, regardless of their composition, exhibited a similar reduction in compressive strength compared to their nonporous versions. This trend highlights the intrinsic trade-offs introduced by porosity, which is critical in scaffold design, where porosity reduces mechanical strength in favor of biological functionality. Neat PLA scaffolds exhibited lower compressive strength compared to ceramic-containing composites. Among the composite scaffolds, PLA-10BBG exhibited the lowest compressive strength, with a slight increase in PLA-10HA-10BBG and PLA-20HA scaffolds.

The range of compressive strengths observed in the porous scaffolds (8.4–10.9 MPa) falls well within the range for cancellous bone (0.1–16 MPa).[66,87] This makes them suitable candidates for applications in bone repair and regeneration, especially in areas where structural integrity and gradual integration with native bone are critical for successful healing.[88] Overall, these findings indicate that ceramic inclusions, particularly HA, enhance compressive strength and provide mechanical compatibility for physiological environments requiring cancellous bone-like support.

As shown in Table 3, the Young's modulus of the PLA-based scaffolds follows a trend similar to that of compressive strength. The incorporation of HA increased

Table 3. The Young's moduli of non-porous scaffolds

Scaffolds	Young's modulus (MPa)	
	Porosity (%)	Medium pore size
PLA	853.8 ± 63.4	84.8 ± 4.1
PLA-10HA	1016.2 ± 52.2	198.4 ± 5.7
PLA-10HA10BBG	929.4 ± 57.2	107.4 ± 3.8
PLA-10BBG	905.4 ± 48.6	96.6 ± 4.7
PLA-20BBG	966.1 ± 62.9	120.8 ± 6.2

Abbreviations: BBG, bioactive borate glass; HA, hydroxyapatite; PLA, polylactic acid.

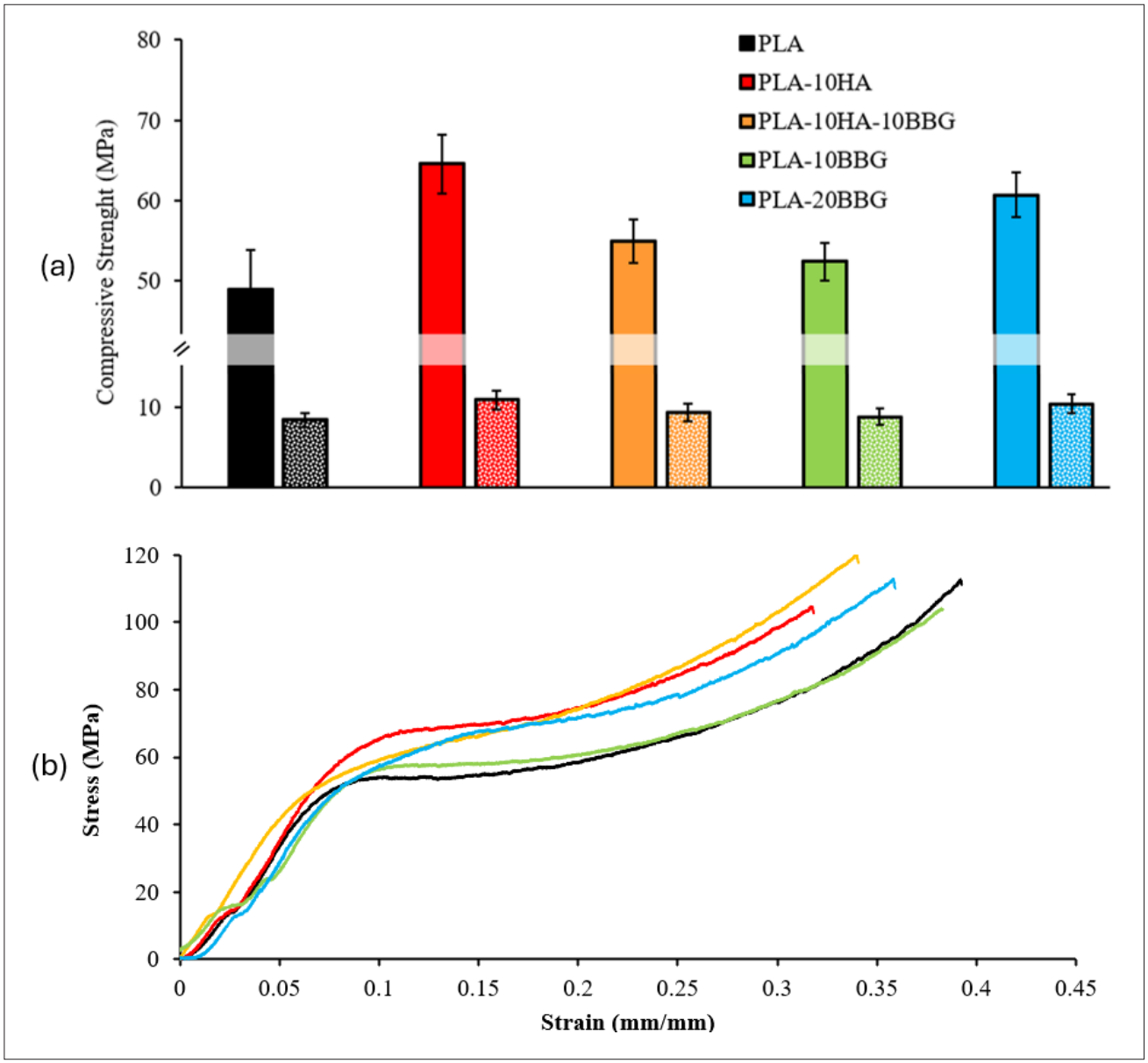

Figure 9. Mechanical properties of the samples. (a) Compressive strength of scaffolds: solid bars are non-porous blocks fabricated with different material compositions indicated, and dotted bars are medium pore scaffolds fabricated with the corresponding material compositions. (b) Stress–strain curves for non-porous scaffolds (number of replicates = 5). Abbreviations: BBG, bioactive borate glass; HA, hydroxyapatite; PLA, polylactic acid.

the modulus from 853.8 ± 63.4 MPa (PLA) to 1016.2 ± 52.2 MPa (PLA-10HA), indicating improved stiffness due to the reinforcement effect of HA particles. The addition of BBG, while still enhancing the modulus, had a less pronounced effect, with values of 905.4 ± 48.6 MPa (PLA-10BBG) and 966.1 ± 62.9 MPa (PLA-20BBG). The combined addition of HA and BBG (PLA-10HA-10BBG) resulted in an intermediate modulus of 929.4 ± 57.2 MPa. The increase in stiffness can be attributed to the ceramic fillers restricting the movement of polymer chains, reinforcing the composite structure. A similar trend was observed in medium-pore (M) scaffolds, where Young's modulus ranged from 84.8 MPa (PLA) to 198.4 MPa (PLA-10HA).

Representative stress–strain curves for non-porous (NP) scaffolds (Figure 9b) illustrate the mechanical response under compressive loading, showing distinct deformation behaviors across different compositions.

3.4. Contact angle

The wettability of the PLA/HA/BBG scaffolds was studied by measuring contact angles with water. Contact angles less than 90° indicate hydrophilic properties, increased wettability, and surface affinity for water.[89] This may enhance cellular adhesion and tissue integration. PLA/HA/BBG scaffolds exhibited hydrophilic behavior with contact angles ranging from 69.7° ± 4° to 81.4° ± 5.3° (Figure 10). In neat PLA, a contact angle of 79.7° ± 4.2° was recorded, consistent with a prior reported value (80.2° ± 3.4°).[90] This is consistent with the low wettability of PLA. The addition of HA did not significantly change the contact angle, with any variations among the PLA-10HA scaffolds falling within the experimental error. Despite its hydrophilic properties, HA did not significantly affect the overall wettability of PLA when added alone. In contrast, the addition of BBG notably decreased the water contact angle, particularly in the PLA-20BBG scaffolds, which exhibited the lowest contact angle at 69.7° ± 4°. This enhanced wettability is likely attributable to the intrinsic surface characteristics of BBG, which increased water affinity and surface energy. The incorporation of BBG into both PLA and PLA-10HA composites resulted in a reduction in contact angles (74.9° ± 5.1° for PLA-10BBG and 73.5° ± 4.4° for PLA-10HA-10BBG), suggesting that BBG is more effective than HA alone in enhancing surface hydrophilicity.[91] These findings align with previous research reports that PCL scaffolds containing BBG exhibited higher wettability and superior green fluorescent protein adsorption compared to neat PCL scaffolds.[55] Consequently, BBG-enriched PLA composites are promising scaffold materials, given their ability to provide biocompatibility and cell-supportive surfaces.[91]

3.5. Bioactivity and biodegradation profile

Figure 11 shows the surface morphology of PLA-based scaffolds after 4 weeks immersion in SBF. Analysis of surface precipitates by EDS confirmed the presence of Ca and P, the main elements of apatite as shown in Table 4. The scaffolds remained untreated after removal from SBF to preserve the morphology of the secondary layer. EDS analysis was performed to identify surface elements, indicating residual salt deposits from SBF evaporation. Micrographs and EDS from Figure 11 and Table 4 revealed higher and varying degrees of apatite formation on the surfaces of PLA scaffolds containing HA and BBG. Apatite formation is primarily influenced by the presence of Ca and

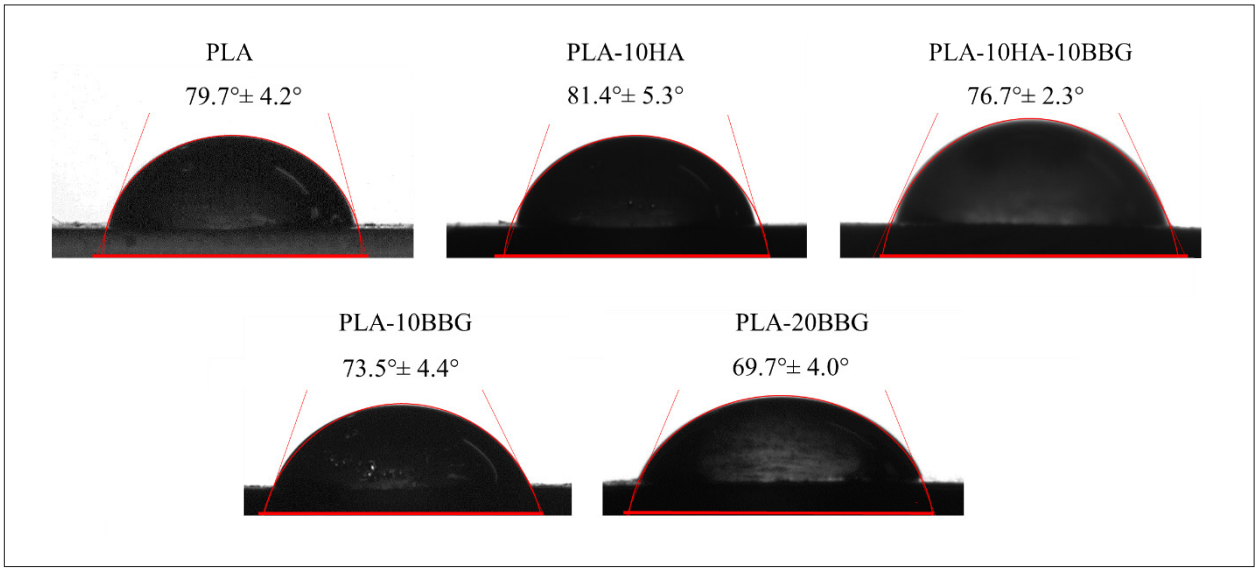

Figure 10. Images and results of water contact angle measurements for PLA PLA-10HA, PLA-10HA-10BBG, PLA-10BBG, and PLA-20BBG scaffolds (number of replicates = 5). Abbreviations: BBG, bioactive borate glass; HA, hydroxyapatite; PLA, polylactic acid.

P on the scaffold surfaces, especially on PLA-10HA, PLA-10HA-10BBG, and PLA-20BBG scaffolds.[92] Incorporation of HA and BBG into PLA scaffolds enhances bioactivity and consequent biomineralization, as calcium phosphate compounds are critical for mimicking the mineral content of natural bone tissue. Ca/P atomic ratios were calculated by dividing the atomic percentages of Ca and P on the scaffold surfaces after 4-week immersion in SBF, providing insights into mineralization and assessment of calcium phosphate compound formation.[93] The Ca/P ratios for the scaffolds were 12.22 for neat PLA, 1.87 for PLA-10HA, 0.97 for PLA-10HA-10BBG, 2.46 for PLA-10BBG, and 2.19 for PLA-20BBG.

Neat PLA scaffolds exhibit a highly hydrophobic nature due to nonpolar methyl (CH_3) side groups and ester (COOR) functional groups, which limit hydrogen bonding with water molecules. This results in low surface energy, reducing the likelihood of immediate interaction with aqueous solutions such as SBF. Additionally, PLA lacks hydroxyl or phosphate groups that would otherwise

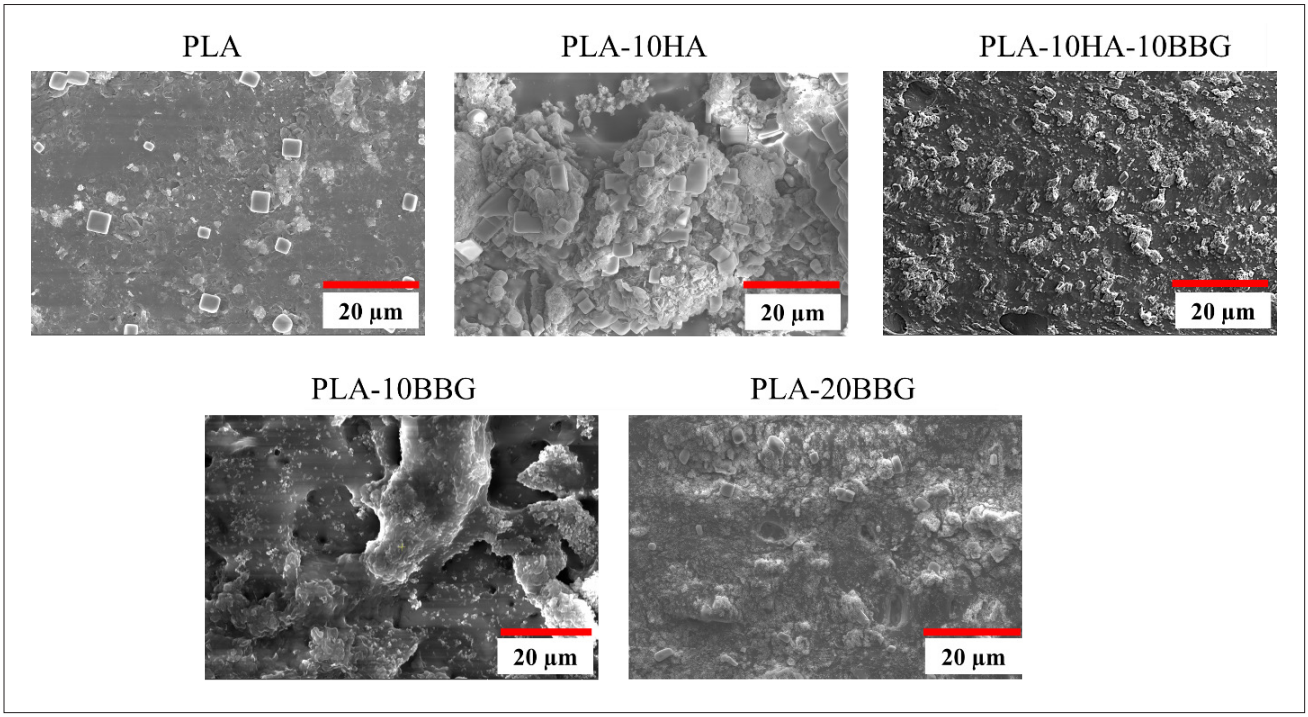

Figure 11. SEM micrographs of PLA-based scaffolds (PLA, PLA-10HA, PLA-10HA-10BBG, PLA-10BBG, and PLA-20BBG) after immersion in SBF for 4 weeks. Abbreviations: BBG, bioactive borate glass; HA, hydroxyapatite; PLA, polylactic acid; SEM, scanning electron microscopy; SBF, simulated body fluid.

Table 4. Scaffolds' surface EDS after 4 weeks of immersion in SBF

Element (wt.%)	PLA	PLA-10HA	PLA-10HA-10BBG	PLA-10BBG	PLA-20BBG
C	44.31 ± 2.32	19.42 ± 3.30	43.62 ± 4.45	36.05 ± 1.90	31.60 ± 3.25
O	41.30 ± 3.47	27.44 ± 2.94	48.61 ± 4.37	46.14 ± 4.28	35.30 ± 5.40
Na	2.40 ± 0.91	8.73 ± 1.09	2.51 ± 0.59	2.11 ± 1.96	8.46 ± 7.09
CL	2.57 ± 1.59	17.27 ± 2.28	1.14 ± 0.20	3.16 ± 1.71	6.57 ± 5.63
P	0.31 ± 0.39	8.15 ± 3.69	1.82 ± 0.52	1.98 ±0 .39	3.60 ± 1.08
Ca	3.79 ± 0.60	15.24 ± 2.13	1.77 ± 0.71	4.86 ± 0.83	7.89 ± 3.56
Others	5.32 ± 0.68	3.75 ± 2.15	0.52 ± 0.08	5.71 ± 3.07	6.58 ± 7.92
Ca/P	12.22	1.87	0.97	2.46	2.19

Note: Number of replicates = 5.

Abbreviations: BBG, bioactive borate glass; EDS, energy-dispersive X-ray spectroscopy; HA, hydroxyapatite; PLA, polylactic acid.

act as nucleation sites for calcium phosphate precipitation. Consequently, in the absence of such functional groups, ion exchange with the surrounding solution is negligible, preventing the direct formation of HA or calcium phosphate mineral phases. Instead, the observed cubic morphology (Figure 11) is characteristic of face centered cubic (FCC) NaCl or orthorhombic $CaCl_2$,[94–96] both of which are common salts present in SBF, which is a supersaturated solution mimicking blood plasma with approximately 9% NaCl content. This interpretation is further supported by the EDS results: (1) high C and O signals, indicating incomplete crystallization and the presence of an exposed polymer surface with no secondary mineral phase, and (2) relatively high Ca, Cl, and Na content but low P levels, further suggesting that the deposits are SBF-derived salts rather than HA. This justifies the unusually high Ca/P ratio observed in neat PLA, which is attributed to the absence of secondary apatite formation. PLA-10HA scaffolds exhibited a Ca/P ratio of 1.87, which deviates slightly from the stoichiometric ratio of HA (1.67). Scaffolds with Ca/P ratios near 1.67 are particularly suitable for BTE, as they closely mimic the mineral composition of native bone. The PLA-10BBG and PLA-20BBG scaffolds exhibited Ca/P ratios of 2.46 and 2.19, respectively, indicating a higher calcium content. These values exceed the ideal stoichiometry of HA, suggesting formation of secondary phases such as CaO, calcium-rich amorphous phases, or incomplete phosphate incorporation within predominantly HA matrix.[97] Incorporating HA and BBG into PLA scaffolds enhances bioactivity by promoting calcium phosphate compound formation, which is crucial for mimicking bone mineral composition.[98,99] These findings suggest that PLA-10HA, PLA-10BBG, and PLA-20BBG scaffolds have strong potential for bone repair, as their surfaces promote mineral formation closely resembling mineral component of natural bone, supporting improved biocompatibility and tissue integration.

Scaffold degradation is a critical factor determining its suitability in biological applications. A low degradation rate can limit tissue regeneration by restricting space for new tissue growth, while rapid degradation may lead to premature scaffold failure before sufficient tissue formation.[34,100] In BTE, controlling the degradation rate is essential to maintain mechanical support while progressively creating space for new bone tissue. To assess the degradation behavior of PLA-based scaffolds, mass loss over time in SBF solution was measured. Figure 12 depicts the weight loss in the studied scaffolds over time. Among them, PLA-20BBG and neat PLA scaffolds showed the highest degradation rates (weight losses of 28.3% and 26.4%, respectively) over a 14-week period. The addition of BBG, known for its reactivity and rapid degradation, accelerated the breakdown of PLA, highlighting BBG's potential role in tuning the degradation rates of biomaterials to match tissue regeneration needs.[34] Neat PLA's elevated weight loss primarily occurs through hydrolytic degradation due to inherent susceptibility of ester bonds to attack by water molecules. This process begins with the diffusion of water into the polymer matrix, where it cleaves the ester linkages, generating shorter polymer chains, carboxyl groups, and hydroxyl-terminated fragments. The presence of acidic carboxyl groups accelerates hydrolysis, ultimately leading to the release of lactic acid as the main degradation product, progressively reducing molecular weight and mechanical integrity over time. Incorporating HA into the PLA scaffolds significantly slowed the degradation rate. The PLA-10HA and PLA-10HA-10BBG scaffolds exhibited lower mass losses of 18.3% and 20.2%, respectively. HA, being highly stable and insoluble in aqueous environments, reduces water uptake and acts as a physical barrier within the polymer matrix, slowing hydrolysis and preserving structural integrity. However, prolonged structural stability could potentially delay scaffold resorption, affecting the rate of tissue regeneration in certain contexts.[101] In contrast to HA, BBG is highly reactive and dissolves upon immersion in SBF, releasing ions such as Ca^{2+}, B^{3+}, and Na^{+}, which alter the local pH and ionic strength, further accelerating the PLA hydrolysis. Furthermore, contact angle measurements indicate that HA decreases surface wettability, reducing water penetration, and thereby delaying hydrolytic degradation, whereas BBG improves wettability, facilitating water diffusion, and accelerating degradation. Therefore, achieving an optimal degradation profile requires balancing HA and BBG content within the PLA matrix. BBG enhances bioactivity and scaffold resorption, whereas HA provides long-term mechanical support, enabling a tunable degradation profile, balancing mechanical support with controlled biodegradation to synchronize it with new tissue formation.

3.6. Biocompatibility

The MTT assay results presented in Figure 13 evaluate the *in vitro* cell viability in contact with HA, BBG, and 3D-printed PLA-based scaffolds using MG63 osteoblast-like cell line over a 7-day extraction period. The assay measures the metabolic activity of cells, directly correlating to cell viability and scaffold biocompatibility. According to ISO 10993-5:2009, which provides guidelines for *in vitro* cytotoxicity testing, a material is considered cytotoxic if it reduces cell viability by more than 30%, meaning that samples with viability above 70% are deemed non-cytotoxic. The results indicate that all scaffold compositions, including neat PLA and HA- or BBG-enriched variants, maintain cell viability above this threshold, confirming their non-cytotoxic nature. PLA-10HA scaffolds exhibited

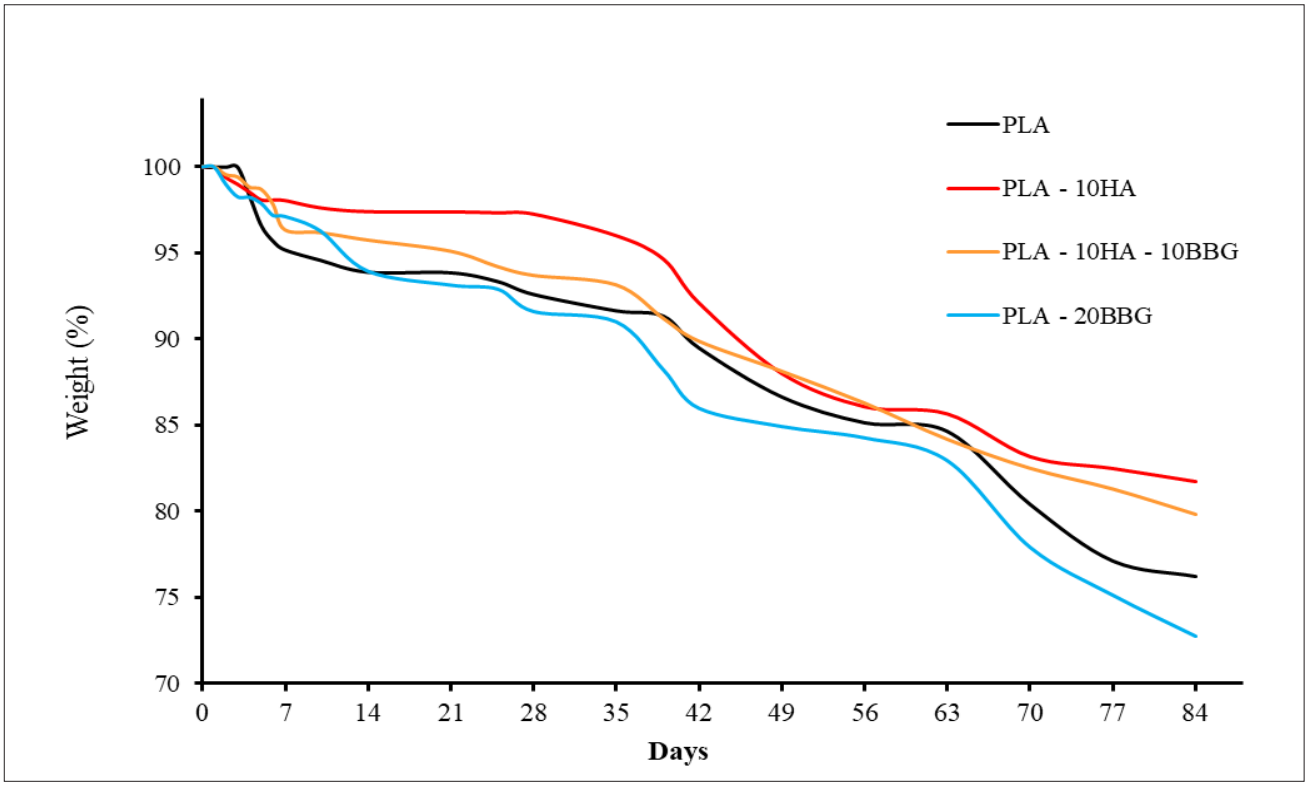

Figure 12. Degradation rate of PLA-based scaffolds (number of replicates = 3). Abbreviations: BBG, bioactive borate glass; HA, hydroxyapatite; PLA, polylactic acid.

the highest cell viability ($p > 0.05$), followed by HA powder, suggesting strong osteoconductive properties of this sample. HA closely mimics the mineral composition of natural bone, providing a calcium and phosphate-rich surface that facilitates the adsorption of proteins and cell adhesion molecules, which are essential for osteoblast attachment, proliferation, and differentiation.[102] The presence of HA promotes the formation of a bone-like apatite layer on the scaffold surface upon immersion in physiological environment, further improving its ability to integrate with surrounding bone tissue.[13,14] Furthermore, the moderate wettability of PLA-10HA scaffolds (~74.9° contact angle) allows for better protein adsorption compared to neat PLA, facilitating cell attachment and growth. Unlike BBG-containing scaffolds, which release high concentrations of ions that can transiently alter local pH and induce oxidative stress, HA degrades more slowly, providing long-term structural integrity and sustained bioactivity without cytotoxic effects. This balance between bioactivity, structural stability, and cell-supportive characteristics makes PLA-10HA scaffolds highly promising for BTE applications.

In contrast, PLA-10BBG and PLA-20BBG scaffolds demonstrated slightly lower viability than PLA-10HA, though they remained within the biocompatible range. The impact of BBG on cell viability is closely linked to its ionic dissolution profile and the subsequent biological interactions. BBG rapidly releases ions such as Ca^{2+} and Na^{+} into the surrounding medium, influencing the local microenvironment and cellular responses.[40,103] A controlled level of ionic dissolution has been shown to enhance osteogenic differentiation and angiogenesis by activating pathways, such as the PI3K/Akt and MAPK/ERK pathways.[104] However, excessive and rapid release of these ions can transiently elevate the local osmotic pressure and pH, creating a hypertonic environment that may induce oxidative stress.[105] This phenomenon explains the slightly lower cell viability observed in PLA-10BBG and PLA-20BBG scaffolds compared to PLA-10HA. While BBG can enhance bone regeneration by stimulating osteogenic gene expression, its rapid degradation profile necessitates careful optimization of its content to balance bioactivity with cell compatibility.[106] Furthermore, BBG's relatively fast dissolution can contribute to localized hypoxia, where cells experience transient stress due to rapid ion exchange disrupting homeostasis. The influx of Ca^{2+} and BO_3^{3+} ions can modulate hypoxia-inducible factor 1-alpha (HIF-1α) stabilization, a key regulator of cellular adaptation under stress conditions.[107] While

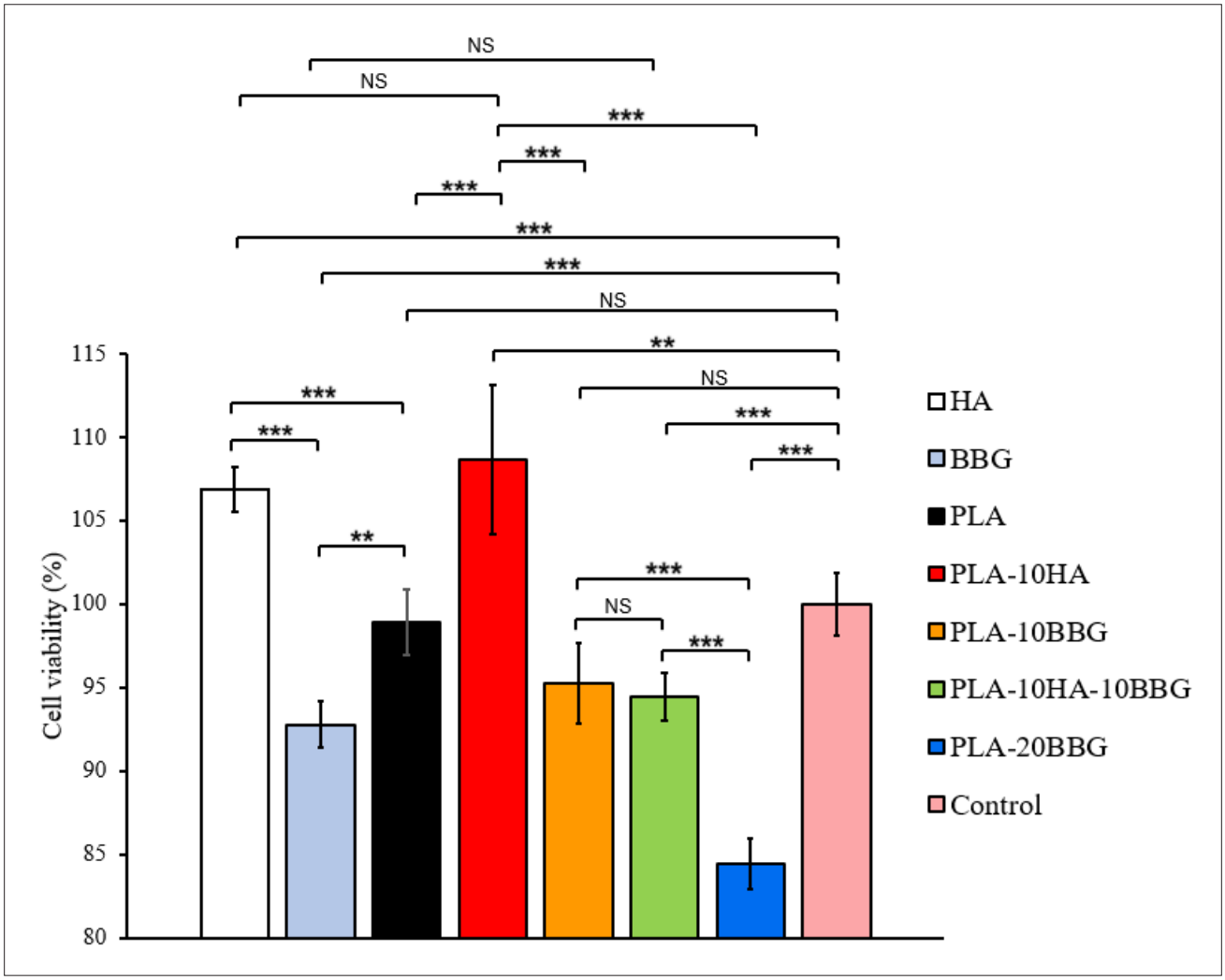

Figure 13. *In vitro* cell viability of HA, BBG, and 3D-printed PLA scaffolds using MG63 cells. All samples indicated 7-day biocompatibility. PLA-10 HA scaffolds exhibited the highest cell viability, followed by HA powder and PLA-BBG20 showed the lowest cell viability followed by BBG powder. All samples showed a toxicity level lower than 30%, which is the toxicity threshold per ISO 10993-5. Statistical significance for comparisons is denoted by $*p < 0.05$, $**p < 0.01$, $***p < 0.001$, and NS as $p > 0.05$ (number of replicates = 6). Abbreviations: BBG, bioactive borate glass; HA, hydroxyapatite; PLA, polylactic acid.

moderate upregulation of HIF-1α is beneficial for angiogenesis and osteogenesis, excessive ionic stress may impair mitochondrial function, reducing ATP production and leading to oxidative damage.[108] The reduced cell viability in PLA-20BBG compared to PLA-10BBG could be attributed to this effect, as a higher BBG content may lead to an imbalance in the rate of ion dissolution relative to cell adaptation. However, despite these minor reductions in cell viability, all scaffolds remained within the biocompatible range, as demonstrated by cell viability greater than 70%. PLA-10HA-10BBG scaffolds showed intermediate cell viability between PLA-10HA and PLA-10BBG. This suggests a synergistic effect of combining HA and BBG, where the osteoconductivity of HA complements the ionic bioactivity of BBG. The balance between the two bioactive materials may create a favorable microenvironment for cell attachment and proliferation.

4. Conclusion

This study investigated the feasibility of fabricating PLA-based bone scaffolds enriched with HA and BBG by DLP 3D printing. HA enhanced PLA's mechanical properties and bioactivity by increasing compressive strength and promoting calcium phosphate deposition. However, the wettability of the PLA-based scaffolds decreased with the incorporation of HA. The addition of BBG to PLA and PLA-HA decreased the viscosity of resin slurry, improving printability and wettability. Thermal analysis showed slight deviations but the overall good agreement between

the intended and actual contents of incombustibles in the printed scaffolds. The secondary apatite formation on PLA scaffolds incorporating HA and BBG was enhanced in comparison to neat PLA. *In vitro* biocompatibility studies confirmed that all scaffold compositions were non-toxic to MG63 cells, with PLA-10HA scaffolds achieving the highest cellular activity. The combination of HA and BBG yields a balance between structural stability and bioactivity, with HA providing prolonged mechanical support and BBG enabling accelerated biodegradation and active ion release. Future studies will focus on advanced biocompatibility assessments, enzymatic activity assays, wet mechanical properties, and *in vitro* and *in vivo* biomineralization, to further validate the scaffolds' osteogenic potential and clinical applicability. Overall, our findings highlight the potential of PLA-based DLP-printed scaffolds to address the limitations of conventional bone grafts by offering a customizable platform for designing scaffolds with controlled porosity that cater to specific clinical requirements for personalized treatment.

Acknowledgments

This work was supported by TÜBİTAK Directorate of Science Fellowships Grant 2214 Programmes (BİDEB) and a seed grant from the Missouri S&T Center for Biomedical Research.

Funding

This work was supported by TÜBİTAK Directorate of Science Fellowships Grant 2214 Programmes (BİDEB) and a seed grant from the Missouri S&T Center for Biomedical Research.

Conflict of interest

Ming Leu serves as the Editorial Board Member of the journal, but did not in any way involve in the editorial and peer-review process conducted for this paper, directly or indirectly. Other authors declare they have no competing interests.

Author contributions

Conceptualization: Engin Gepek, Fateme Fayyazbakhsh, Ming C. Leu

Data curation: Engin Gepek, Fateme Fayyazbakhsh, Lev Suliandziga, Vadym N. Mochalin

Formal analysis: Engin Gepek, Fateme Fayyazbakhsh, Vadym N. Mochalin

Funding acquisition: Fateme Fayyazbakhsh, Osman Iyibilgin, Ming C. Leu

Investigation: Fateme Fayyazbakhsh, Vadym N. Mochalin, Osman Iyibilgin, Yue-Wern Huang, Ming C. Leu

Methodology: Engin Gepek, Fateme Fayyazbakhsh, Vadym N. Mochalin, Ming C. Leu

Project administration: Fateme Fayyazbakhsh, Ming C. Leu

Resources: Fateme Fayyazbakhsh, Vadym N. Mochalin, Yue-Wern Huang, Ming C. Leu

Supervision: Fateme Fayyazbakhsh, Ming C. Leu

Validation: Fateme Fayyazbakhsh, Vadym N. Mochalin, Ming C. Leu

Visualization: Engin Gepek, Fateme Fayyazbakhsh

Writing – original draft: Engin Gepek, Fateme Fayyazbakhsh

Writing – review & editing: Vadym N. Mochalin, Yue-Wern Huang, Ming C. Leu

Ethics approval and consent to participate

Not applicable.

Consent for publication

Not applicable.

Availability of data

Raw data are available to readers upon reasonable request to the corresponding author.

References

1. Xue N, Ding X, Huang R, et al. Bone tissue engineering in the treatment of bone defects. *Pharmaceuticals*. 2022;15(7):879.
doi: 10.3390/ph15070879

2. Zhang W, Jiang Z, Chi J, et al. A novel porous butyryl chitin–animal derived hydroxyapatite composite scaffold for cranial bone defect repair. *Int J Mol Sci*. 2023;24(10):8519.
doi: 10.3390/ijms24108519

3. Wei H, Cui J, Lin K, Xie J, Wang X. Recent advances in smart stimuli-responsive biomaterials for bone therapeutics and regeneration. *Bone Res*. 2022;10(1):17.
doi: 10.1038/s41413-021-00180-y

4. Omar O, Engstrand T, Linder LKB, et al. In situ bone regeneration of large cranial defects using synthetic ceramic implants with a tailored composition and design. *Proc Natl Acad Sci U S A*. 2020;117(43):26660-26671.
doi: 10.1073/pnas.2007635117

5. Xu W, Pranovich A, Uppstu P, et al. Novel biorenewable composite of wood polysaccharide and polylactic acid for three dimensional printing. *Carbohydr Polym*. 2018;187(January):51-58.
doi: 10.1016/j.carbpol.2018.01.069

6. Gillman CE, Jayasuriya AC. FDA-approved bone grafts and bone graft substitute devices in bone regeneration. *Mater Sci Eng C*. 2021;130(July):112466.
doi: 10.1016/j.msec.2021.112466

7. Wang W, Yeung KWK. Bone grafts and biomaterials substitutes for bone defect repair: a review. *Bioact Mater*. 2017;2(4):224-247. doi: 10.1016/j.bioactmat.2017.05.007

8. Fernandez de Grado G, Keller L, Idoux-Gillet Y, et al. Bone substitutes: a review of their characteristics, clinical use, and perspectives for large bone defects management. *J Tissue Eng*. 2018;9:2041731418776819. doi: 10.1177/2041731418776819

9. Oryan A, Alidadi S, Moshiri A. Current concerns regarding healing of bone defects. *Hard Tissue*. 2013;2(2);13. doi: 10.13172/2050-2303-2-2-374

10. Murphy CM. Understanding the effect of mean pore size on cell activity in collagen-glycosaminoglycan scaffolds. *Cell Adh Migr*. 2010;4(3):377-381. doi: 10.4161/cam.4.3.11747

11. Sobral JM, Caridade SG, Sousa RA, Mano JF, Reis RL. Three-dimensional plotted scaffolds with controlled pore size gradients : Effect of scaffold geometry on mechanical performance and cell seeding efficiency. *Acta Biomater*. 2011;7:1009-1018. doi: 10.1016/j.actbio.2010.11.003

12. Abbasi N, Hamlet S, Love RM, Nguyen NT. Porous scaffolds for bone regeneration. *J Sci: Adv Mater Devices*. 2020;5(1):1-9. doi: 10.1016/j.jsamd.2020.01.007

13. Fayyazbakhsh F, Solati-Hashjin M, Keshtkar A, Shokrgozar MA, Dehghan MM, Larijani B. Novel layered double hydroxides-hydroxyapatite/gelatin bone tissue engineering scaffolds: fabrication, characterization, and in vivo study. *Mater Sci Eng C*. 2017;76:701-714. doi: 10.1016/j.msec.2017.02.172

14. Fayyazbakhsh F, Solati-Hashjin M, Keshtkar A, Shokrgozar MA, Dehghan MM, Larijani B. Release behavior and signaling effect of vitamin D3 in layered double hydroxides-hydroxyapatite/gelatin bone tissue engineering scaffold: an in vitro evaluation. *Colloids Surf B Biointerfaces*. 2017;158:697-708. doi: 10.1016/j.colsurfb.2017.07.004

15. Chinnasami H, Dey MK, Devireddy R. Three-dimensional scaffolds for bone tissue engineering. *Bioengineering (Basel)*. 2023;10(7):759. doi: 10.3390/bioengineering10070759

16. Adel IM, Elmeligy MF, Elkasabgy NA. Conventional and recent trends of scaffolds fabrication: a superior mode for tissue engineering. *Pharmaceutics*. 2022;14(2):306. doi: 10.3390/pharmaceutics14020306

17. Percival KM, Paul V, Husseini GA. Recent advancements in bone tissue engineering: integrating smart scaffold technologies and bio-responsive systems for enhanced regeneration. *Int J Mol Sci*. 2024;25(11):6012. doi: 10.3390/ijms25116012

18. Nayak VV, Sanjairaj V, Behera RK, et al. Direct inkjet writing of polylactic acid/β-tricalcium phosphate composites for bone tissue regeneration: a proof-of-concept study. *J Biomed Mater Res B Appl Biomater*. 2024;112(4):e35402. doi: 10.1002/jbm.b.35402

19. Ait Said H, Mabroum H, Lahcini M, et al. Manufacturing methods, properties, and potential applications in bone tissue regeneration of hydroxyapatite-chitosan biocomposites: a review. *Int J Biol Macromol*. 2023;243:125150. doi: 10.1016/j.ijbiomac.2023.125150

20. Aytac Z, Dubey N, Daghrery A, et al. Innovations in craniofacial bone and periodontal tissue engineering–from electrospinning to converged fabrication. *Int Mater Rev*. 2022;67(4):347-384. doi: 10.1080/09506608.2021.1946236

21. Germaini MM, Belhabib S, Guessasma S, Deterre R, Corre P, Weiss P. Additive manufacturing of biomaterials for bone tissue engineering – a critical review of the state of the art and new concepts. *Prog Mater Sci*. 2022;130:100963. doi: 10.1016/j.pmatsci.2022.100963

22. Mok SW, Nizak R, Fu SC, et al. From the printer: potential of three-dimensional printing for orthopaedic applications. *J Orthop Translat*. 2016;6:42-49. doi: 10.1016/j.jot.2016.04.003

23. Zadpoor AA. Bone tissue regeneration: the role of scaffold geometry. *Biomater Sci*. 2015;3(2):231-245. doi: 10.1039/c4bm00291a

24. Cheah CM, Chua CK, Leong KF, Cheong CH, Naing MW. Automatic algorithm for generating complex polyhedral scaffold structures for tissue engineering. *Tissue Eng*. 2004;10(3-4):595-610. doi: 10.1089/107632704323061951

25. Chua CK, Leong KF, Cheah CM, Chua SW. Development of a tissue engineering scaffold structure library for rapid prototyping. Part 1: investigation and classification. *Int J Adv Manuf Technol*. 2003;21(4):291-301. doi: 10.1007/s001700300034

26. Jia Z, Xu X, Zhu D, Zheng Y. Design, printing, and engineering of regenerative biomaterials for personalized bone healthcare. *Prog Mater Sci*. 2023;134:101072. doi: 10.1016/j.pmatsci.2023.101072

27. Kadry H, Wadnap S, Xu C, Ahsan F. Digital light processing (DLP) 3D-printing technology and photoreactive polymers in fabrication of modified-release tablets. *Eur J Pharm Sci*. 2019;135:60-67. doi: 10.1016/j.ejps.2019.05.008

28. Mohammed AA, Algahtani MS, Ahmad MZ, Ahmad J, Kotta S. 3D printing in medicine: technology overview and drug delivery applications. *Ann 3D Printed Med*. 2021;4:100037. doi: 10.1016/j.stlm.2021.100037

29. Lv Y, Wang B, Liu G, et al. Metal material, properties and design methods of porous biomedical scaffolds for

additive manufacturing: a review. *Front Bioeng Biotechnol*. 2021;9:641130.
doi: 10.3389/fbioe.2021.641130

30. Zeng Y, Yan Y, Yan H, et al. 3D printing of hydroxyapatite scaffolds with good mechanical and biocompatible properties by digital light processing. *J Mater Sci*. 2018;53(9):6291-6301.
doi: 10.1007/s10853-018-1992-2

31. İyibilgin O, Gepek E. Additive manufacturing technologies and its future in industrial applications. *Int J Integr Eng*. 2021;13(5):245-257.
doi: 10.30880/ijie.2021.13.07.028

32. Arifin N, Sudin I, Ngadiman NHA, Ishak MSA. A comprehensive review of biopolymer fabrication in additive manufacturing processing for 3D-tissue-engineering scaffolds. *Polymers (Basel)*. 2022;14(10):2119.
doi: 10.3390/polym14102119

33. Yao Q, Cosme JGL, Xu T, et al. Three dimensional electrospun PCL/PLA blend nanofibrous scaffolds with significantly improved stem cells osteogenic differentiation and cranial bone formation. *Biomaterials*. 2017;115:115-127.
doi: 10.1016/j.biomaterials.2016.11.018

34. Fayyazbakhsh F, Khayat MJ, Sadler C, Day D, Huang YW, Leu MC. 3D-printed hydrogels dressings with bioactive borate glass for continuous hydration and treatment of second-degree burns. *Int J Bioprint*. 2023;9(6):0118.
doi: 10.36922/ijb.0118

35. Caroline M, Kolan K, Li W, Semon J, Day D, Leu M. 3D bioprinting of stem cells and polymer/bioactive glass composite scaffolds for bone tissue engineering. *Int J Bioprint*. 2017;3(1):53-63.
doi: 10.18063/IJB.2017.01.005

36. Fayyazbakhsh F, Solati-Hashjin M, Shokrgozar MA, et al. Biological evaluation of a novel tissue engineering scaffold of Layered Double Hydroxides (LDHs). *Key Eng Mater*. 2012;493-494:902-908.
doi: 10.4028/www.scientific.net/KEM.493-494.902

37. Zhang Q, Mochalin VN, Neitzel I, et al. Mechanical properties and biomineralization of multifunctional nanodiamond-PLLA composites for bone tissue engineering. *Biomaterials*. 2012;33(20):5067-5075.
doi: 10.1016/j.biomaterials.2012.03.063

38. Zhang Q, Mochalin VN, Neitzel I, et al. Fluorescent PLLA-nanodiamond composites for bone tissue engineering. *Biomaterials*. 2011;32(1):87-94.
doi: 10.1016/j.biomaterials.2010.08.090

39. Siavashani AZ, Nazarpak MH, Bakhsh FF, Toliyat T, Solati-Hashjin M. Preparation of mesoporous silica nanoparticles for insulin drug delivery. *Adv Mat Res*. 2014;829:251-257.
doi: 10.4028/www.scientific.net/amr.829.251

40. Azari Z, Kermani F, Mollazadeh S, et al. Fabrication and characterization of cobalt- and copper-doped mesoporous borate bioactive glasses for potential applications in tissue engineering. *Ceram Int*. 2023;49(23):38773-38788.
doi: 10.1016/j.ceramint.2023.09.214

41. Liang R, Gu Y, Wu Y, Bunpetch V, Zhang S. Lithography-based 3D bioprinting and bioinks for bone repair and regeneration. *ACS Biomater Sci Eng*. 2021;7(3):806-816.
doi: 10.1021/acsbiomaterials.9b01818

42. Zhang B, Xing F, Chen L, et al. DLP fabrication of customized porous bioceramics with osteoinduction ability for remote isolation bone regeneration. *Biomater Adv*. 2023; 145:213261.
doi: 10.1016/j.bioadv.2022.213261

43. Wang Y, Chen S, Liang H, Liu Y, Bai J, Wang M. Digital light processing (DLP) of nano biphasic calcium phosphate bioceramic for making bone tissue engineering scaffolds. *Ceram Int*. 2022;48(19):27681-27692.
doi: 10.1016/j.ceramint.2022.06.067

44. Ghahri T, Salehi Z, Aghajanpour S, et al. Development of osteon-like scaffold-cell construct by quadruple coaxial extrusion-based 3D bioprinting of nanocomposite hydrogel. *Biomater Adv*. 2023;145:213254.
doi: 10.1016/j.bioadv.2022.213254

45. Alam F, Shukla VR, Varadarajan KM, Kumar S. Microarchitected 3D printed polylactic acid (PLA) nanocomposite scaffolds for biomedical applications. *J Mech Behav Biomed Mater*. 2020;103:103576.
doi: 10.1016/j.jmbbm.2019.103576

46. Li N, Li Y, Liu S. Rapid prototyping of continuous carbon fiber reinforced polylactic acid composites by 3D printing. *J Mater Process Technol*. 2016;238:218-225.
doi: 10.1016/j.jmatprotec.2016.07.025

47. Bernardo MP, da Silva BCR, Hamouda AEI, et al. PLA/Hydroxyapatite scaffolds exhibit in vitro immunological inertness and promote robust osteogenic differentiation of human mesenchymal stem cells without osteogenic stimuli. *Sci Rep*. 2022;12(1):1-15.
doi: 10.1038/s41598-022-05207-w

48. Horvat G, Rožanc J, Maver U, Finšgar M, Knez Ž, Novak Z. Reinforcing ethyl cellulose aerogels with poly(lactic acid) for enhanced bone regeneration. *Cellulose*. 2024;31:4421-4439.
doi: 10.1007/s10570-024-05905-w

49. Hassanajili S, Karami-Pour A, Oryan A, Talaei-Khozani T. Preparation and characterization of PLA/PCL/HA composite scaffolds using indirect 3D printing for bone tissue engineering. *Mater Sci Eng C Mater Biol Appl*. 2019;104:109960.
doi: 10.1016/j.msec.2019.109960

50. Türk S, Altınsoy İ, ÇelebiEfe G, Ipek M, Özacar M, Bindal C. Microwave–assisted biomimetic synthesis of hydroxyapatite using different sources of calcium. *Mater Sci Eng C*. 2017;76:528-535.
doi: 10.1016/j.msec.2017.03.116

51. Rajendran AK, Anthraper MSJ, Hwang NS, Rangasamy J. Osteogenesis and angiogenesis promoting bioactive ceramics. *Mater Sci Eng R: Rep*. 2024;159:100801. doi: 10.1016/j.mser.2024.100801

52. Abodunrin OD, El Mabrouk K, Bricha M. A review on borate bioactive glasses (BBG): effect of doping elements, degradation, and applications. *J Mater Chem B*. 2023;11(5):955-973. doi: 10.1039/d2tb02505a

53. Mistry S, Kundu D, Datta S, Basu D. Comparison of bioactive glass coated and hydroxyapatite coated titanium dental implants in the human jaw bone. *Aust Dent J*. 2011;56(1):68-75. doi: 10.1111/j.1834-7819.2010.01305.x

54. Aslam AA, Akram J, Mehmood RA, et al. Boron-based bioactive glasses: properties, processing, characterization and applications. *Ceram Int*. 2023;49(12):19595-19605. doi: 10.1016/j.ceramint.2023.03.164

55. Han J, Wu J, Xiang X, et al. Biodegradable BBG/PCL composite scaffolds fabricated by selective laser sintering for directed regeneration of critical-sized bone defects. *Mater Des*. 2023;225:111543. doi: 10.1016/j.matdes.2022.111543

56. Turnbull G, Clarke J, Picard F, et al. 3D bioactive composite scaffolds for bone tissue engineering. *Bioact Mater*. 2018;3(3):278-314. doi: 10.1016/j.bioactmat.2017.10.001

57. Ege D, Zheng K, Boccaccini AR. Borate bioactive glasses (BBG): bone regeneration, wound healing applications, and future directions. *ACS Appl Bio Mater*. 2022;5(8):3608-3622. doi: 10.1021/acsabm.2c00384

58. Fayyazbakhsh F, Tusar HM, Huang YW, Leu CM. Effect of bioactive borate glass on printability and physical properties of hydrogels. *Mater Sci Addit Manuf*. 2024;3(1):2845. doi: 10.36922/msam.2845

59. Lin YM, Chen H, Lin CH, Huang PJ, Lee SY. Development of polycaprolactone/hydroxyapatite composite resin for 405 nm digital light projection 3D printing. *Rapid Prototyp J*. 2020;26(5):951-958. doi: 10.1108/RPJ-06-2019-0166

60. Song P, Li M, Zhang B, et al. DLP fabricating of precision GelMA/HAp porous composite scaffold for bone tissue engineering application. *Compos B Eng*. 2022; 244:110163. doi: 10.1016/j.compositesb.2022.110163

61. Gepek E, Fayyazbakhsh F, Iyibilgin O, Suliandziga L, Leu M. PLA-HA/BBG composite scaffolds fabricated by digital-light-processing 3D printing for cranial bone regeneration. In: *Proceedings of the 35th Annual International Solid Freeform Fabrication Symposium – An Additive Manufacturing Conference*. University of Texas at Austin; 2024. doi: 10.26153/tsw/58069

62. Vieira BM, Costa M de O, Thiré RM da S, Araujo AC. Comparison of the porosity of scaffolds manufactured by two additive manufacturing technologies: SLA and FDM. In: *24th ABCM International Congress of Mechanical Engineering*; 2018.

63. Kokubo T, Takadama H. How useful is SBF in predicting *in vivo* bone bioactivity? *Biomaterials*. 2006;27(15): 2907-2915. doi: 10.1016/j.biomaterials.2006.01.017

64. Zhang J, Huang D, Liu S, et al. Zirconia toughened hydroxyapatite biocomposite formed by a DLP 3D printing process for potential bone tissue engineering. *Mater Sci Eng C*. 2019;105:110054. doi: 10.1016/j.msec.2019.110054

65. Xu X, Zhou S, Wu J, Zhang C, Liu X. Inter-particle interactions of alumina powders in UV-curable suspensions for DLP stereolithography and its effect on rheology, solid loading, and self-leveling behavior. *J Eur Ceram Soc*. 2021;41(4):2763-2774. doi: 10.1016/j.jeurceramsoc.2020.12.004

66. Wu D, Spanou A, Diez-Escudero A, Persson C. 3D-printed PLA/HA composite structures as synthetic trabecular bone: a feasibility study using fused deposition modeling. *J Mech Behav Biomed Mater*. 2020;103:103608. doi: 10.1016/j.jmbbm.2019.103608

67. Tanase-Opedal M, Espinosa E, Rodríguez A, Chinga-Carrasco G. Lignin: a biopolymer from forestry biomass for biocomposites and 3D printing. *Materials*. 2019; 12(18):3006. doi: 10.3390/ma12183006

68. Nim B, Rahayu SS, Thananukul K, et al. Sizing down and functionalizing polylactide (PLA) resin for synthesis of PLA - based polyurethanes for use in biomedical applications. *Sci Rep*. 2023;13(1):2284. doi: 10.1038/s41598-023-29496-x

69. Liu S, Zheng Y. Preparation and characterization of a novel polylactic acid / hydroxyapatite composite scaffold with biomimetic micro-nano fi brous porous structure. *J Mater Sci Mater Med*. 2020;31(8):74. doi: 10.1007/s10856-020-06415-4

70. Mofokeng JP, Luyt AS, Tábi T, Kovács J. Comparison of injection moulded, natural fibre-reinforced composites with PP and PLA as matrices. *J Thermoplastic Compos Mater*. 2012;25(8):927-948. doi: 10.1177/0892705711423291

71. González-Benito J, Zuñiga-Prado S, Najera J, Olmos D. Non-woven fibrous polylactic acid/hydroxyapatite nanocomposites obtained via solution blow spinning: morphology, thermal and mechanical behavior. *Nanomaterials*. 2024;14(2):196. doi: 10.3390/nano14020196

72. Alam K, Gafur MA, Md. Hasan Mahmud KAS. Chemical characteristics of hydroxyapatite from oyster shell by

thermo-chemical process. *Int J Innov Res Sci Eng Technol*. 2015;04(07):5039-5047.
doi: 10.15680/IJIRSET.2015.0407002

73. Umapathi R, Lim JH. Effect of infill pattern and lattice structure on the mechanical properties of 3d printed metal polylactide filament. *J Phys Conf Ser*. 2021;2120(1):012019.
doi: 10.1088/1742-6596/2120/1/012019

74. Vu MC, Jeong T, Kim J, Choi WK, Kim DH, Kim S. 3D printing of copper particles and poly(methyl methacrylate) beads containing poly(lactic acid) composites for enhancing thermomechanical properties. *J Appl Polym Sci*. 2021;138(5):1-10.
doi: 10.1002/app.49776

75. Ruz-Cruz MA, Herrera-Franco PJ, Flores-Johnson EA, Moreno-Chulim MV, Galera-Manzano LM, Valadez-González A. Thermal and mechanical properties of PLA-based multiscale cellulosic biocomposites. *J Mater Res Technol*. 2022;18:485-495.
doi: 10.1016/j.jmrt.2022.02.072

76. Inkinen S, Hakkarainen M, Albertsson AC, Södergård A. From lactic acid to poly(lactic acid) (PLA): characterization and analysis of PLA and its precursors. *Biomacromolecules*. 2011;12(3):523-532.
doi: 10.1021/bm101302t

77. Akindoyo JO, Beg MDH, Ghazali S, Heim HP, Feldmann M. Impact modified PLA-hydroxyapatite composites – thermo-mechanical properties. *Compos Part A Appl Sci Manuf*. 2018;107:326-333.
doi: 10.1016/j.compositesa.2018.01.017

78. El-Hajje A, Kolos EC, Wang JK, et al. Physical and mechanical characterisation of 3D-printed porous titanium for biomedical applications. *J Mater Sci Mater Med*. 2014;25(11):2471-2480.
doi: 10.1007/s10856-014-5277-2

79. Koushik TM, Miller CM, Antunes E. Bone tissue engineering scaffolds: function of multi-material hierarchically structured scaffolds. *Adv Healthc Mater*. 2023;12(9):e2202766.
doi: 10.1002/adhm.202202766

80. Liu K, Zhou C, Hu J, et al. Fabrication of barium titanate ceramics via digital light processing 3D printing by using high refractive index monomer. *J Eur Ceram Soc*. 2021;41(12):5909-5917.
doi: 10.1016/j.jeurceramsoc.2021.04.044

81. Liang H, Wang Y, Chen S, Liu Y, Liu Z, Bai J. Nano-hydroxyapatite bone scaffolds with different porous structures processed by digital light processing 3D printing. *Int J Bioprint*. 2022;8(1):198-210.
doi: 10.18063/IJB.V8I1.502

82. Zhang Q, Weng S, Hamel CM, et al. Design for the reduction of volume shrinkage-induced distortion in digital light processing 3D printing. *Extreme Mech Lett*. 2021;48:101403.
doi: doi: 10.1016/j.eml.2021.101403

83. Jian Y, He Y, Jiang T, Li C, Yang W, Nie J. Polymerization shrinkage of (Meth) acrylate determined by reflective laser beam scanning. *J Polym Sci B Polym Phys*. 2012;50:923-928.
doi: 10.1002/polb.23086

84. Jaidev LR, Chatterjee K. Surface functionalization of 3D printed polymer scaffolds to augment stem cell response. *Mater Des*. 2019;161:44-54.
doi: 10.1016/j.matdes.2018.11.018

85. Mu M, Liu S, DeFlorio W, et al. Influence of surface roughness, nanostructure, and wetting on bacterial adhesion. *Langmuir*. 2023;39(15):5426-5439.
doi: 10.1021/acs.langmuir.3c00091

86. Subramaniyan M, Karuppan S, Helaili S, Ahmad I. Structural, mechanical, and in-vitro characterization of hydroxyapatite loaded PLA composites. *J Mol Struct*. 2024;1306:137862.
doi: 10.1016/j.molstruc.2024.137862

87. Gerhardt LC, Boccaccini AR. Bioactive glass and glass-ceramic scaffolds for bone tissue engineering. *Materials*. 2010;3(7):3867-3910.
doi: 10.3390/ma3073867

88. Darghiasi SF, Farazin A, Ghazali HS. Design of bone scaffolds with calcium phosphate and its derivatives by 3D printing: a review. *J Mech Behav Biomed Mater*. 2024;151:106391.
doi: 10.1016/j.jmbbm.2024.106391

89. Abushahba F, Tuukkanen J, Aalto-Setälä L, Miinalainen I, Hupa L, Närhi TO. Effect of bioactive glass air-abrasion on the wettability and osteoblast proliferation on sandblasted and acid-etched titanium surfaces. *Eur J Oral Sci*. 2020;128(2):160-169.
doi: 10.1111/eos.12683

90. Nazeer MA, Onder OC, Sevgili I, Yilgor E, Kavakli IH, Yilgor I. 3D printed poly(lactic acid) scaffolds modified with chitosan and hydroxyapatite for bone repair applications. *Mater Today Commun*. 2020;25:101515.
doi: 10.1016/j.mtcomm.2020.101515

91. Donate R, Monzón M, Alemán-Domínguez ME. Additive manufacturing of PLA-based scaffolds intended for bone regeneration and strategies to improve their biological properties. *E-Polymers*. 2020;20(1):571-599.
doi: 10.1515/epoly-2020-0046

92. Manzoor F, Golbang A, Jindal S, et al. 3D printed PEEK/HA composites for bone tissue engineering applications: effect of material formulation on mechanical performance and bioactive potential. *J Mech Behav Biomed Mater*. 2021;121:104601.
doi: 10.1016/j.jmbbm.2021.104601

93. Amaravathy P, Kumar TSSS. Bioactivity enhancement by Sr doped Zn-Ca-P coatings on biomedical magnesium alloy. *J Mag Alloys*. 2019;7(4):584-596.
doi: 10.1016/j.jma.2019.05.014

94. Hadjittofis E, Vargas SM, Litster JD, Campbell KLS. Exploring the role of crystal habit in the Ostwald rule of

stages. *Proc Math Phys Eng Sci*. 2022;478(2258):20210601.
doi: 10.1098/rspa.2021.0601

95. Guo X, Liu L, Wang W, Zhang J, Wang Y, Yu SH. Controlled crystallization of hierarchical and porous calcium carbonate crystals using polypeptide type block copolymer as crystal growth modifier in a mixed solution. *CrystEngComm*. 2011;13(6):2054-2061.
doi: 10.1039/c0ce00202j

96. Cheng H, Zhang X, Song H. Morphological investigation of calcium carbonate during ammonification-carbonization process of low concentration calcium solution. *J Nanomater*. 2014;503696:1-7.
doi: 10.1155/2014/503696

97. Liu H, Yazici H, Ergun C, Webster TJ, Bermek H. An in vitro evaluation of the Ca/P ratio for the cytocompatibility of nano-to-micron particulate calcium phosphates for bone regeneration. *Acta Biomater*. 2008;4(5):1472-1479.
doi: 10.1016/j.actbio.2008.02.025

98. He YH, Zhang YQ, Jiang YH, Zhou R. Microstructure evolution and enhanced bioactivity of Ti-Nb-Zr alloy by bioactive hydroxyapatite fabricated: via spark plasma sintering. *RSC Adv*. 2016;6(103):100939-100953.
doi: 10.1039/c6ra22986g

99. Fiume E, Tulyaganov D, Ubertalli G, Verné E, Baino F. Dolomite-foamed bioactive silicate scaffolds for bone tissue repair. *Materials*. 2020;13(3):1-13.
doi: 10.3390/ma13030628

100. Ma P, Wu W, Wei Y, Ren L, Lin S, Wu J. Biomimetic gelatin/chitosan/polyvinyl alcohol/nano-hydroxyapatite scaffolds for bone tissue engineering. *Mater Des*. 2021; 207:109865.
doi: 10.1016/j.matdes.2021.109865

101. Wang Q, Wang Q, Wan C. Preparation and evaluation of a biomimetic scaffold with porosity gradients in vitro. *An Acad Bras Cienc*. 2012;84(1):9-16.
doi: 10.1590/S0001-37652012005000003

102. Mohammadkhah M, Marinkovic D, Zehn M, Checa S. A review on computer modeling of bone piezoelectricity and its application to bone adaptation and regeneration. *Bone*. 2019;127:544-555.
doi: 10.1016/j.bone.2019.07.024

103. Zhang K, Alaohali A, Sawangboon N, Sharpe PT, Brauer DS, Gentleman E. A comparison of lithium-substituted phosphate and borate bioactive glasses for mineralised tissue repair. *Dent Mater*. 2019;35(6):919-927.
doi: 10.1016/j.dental.2019.03.008

104. Marquardt LM, Day D, Sakiyama-Elbert SE, Harkins AB. Effects of borate-based bioactive glass on neuron viability and neurite extension. *J Biomed Mater Res A*. 2014;102(8):2767-2775.
doi: 10.1002/jbm.a.34944

105. Haro Durand LA, Vargas GE, Romero NM, et al. Angiogenic effects of ionic dissolution products released from a boron-doped 45S5 bioactive glass. *J Mater Chem B*. 2015;3(6):1142-1148.
doi: 10.1039/c4tb01840k

106. Shafaghi R, Rodriguez O, Phull S, et al. Effect of TiO2 doping on degradation rate, microstructure and strength of borate bioactive glass scaffolds. *Mater Sci Eng C*. 2020;107:110351.
doi: 10.1016/j.msec.2019.110351

107. Decker S, Arango-Ospina M, Rehder F, et al. In vitro and in vivo impact of the ionic dissolution products of boron-doped bioactive silicate glasses on cell viability, osteogenesis and angiogenesis. *Sci Rep*. 2022;12(1):8510.
doi: 10.1038/s41598-022-12430-y

108. Luo SH, Xiao W, Wei XJ, et al. In vitro evaluation of cytotoxicity of silver-containing borate bioactive glass. *J Biomed Mater Res B Appl Biomater*. 2010;95B(2):441-448.
doi: 10.1002/jbm.b.31735